EXPERIMENTAL CONSTRAINTS ON THE $^{59}Cu(p,\gamma)^{60}Zn$ REACTION CROSS SECTION FOR ASTROPHYSICAL APPLICATIONS

By

Gerard Jordan A. Owens-Fryar

A DISSERTATION

Submitted to
Michigan State University
in partial fulfillment of the requirements
for the degree of

Physics—Doctor of Philosophy

2026

ABSTRACT

Nuclear astrophysics aims to understand how the stars form chemical elements. Elements of mass greater than 56 are created mainly through the slow and rapid neutron capture processes in neutron dense environments; however, other formation paths exist. Two such paths are the rapid proton capture and neutrino proton capture processes. The site of the rapid proton capture process is on the surface of accreting neutron stars, where light mass material undergoes thermonuclear runaway resulting in a Type I X-ray burst. The neutrino proton capture process can occur in the neutrino driven winds of core collapse super novae.

Investigating the paths these processes follow requires information on the reaction cross sections of a plethora of exotic, radioactive nuclei. As most of these cross sections are unmeasured, modeling the processes relies on theoretical calculations that have large uncertainties on the isotopes in these paths. Therefore, it is imperative that measurements are performed at relevant astrophysical temperatures.

This thesis centers on a common reaction between both the rapid proton and neutrino proton capture processes: $^{59}Cu(p,\gamma)^{60}Zn$. The cross section of this reaction determines whether the path moves more material to higher mass isotopes or if the majority of the material enters the NiCu cycle, near mass 56-60.

The experiment presented here, was performed in 2019 at the National Superconducting Cyclotron Laboratory at Michigan State University. A cocktail beam of isotopes near mass 55 was implanted on a Double Side Silicon Strip Detector positioned in the center of the Summing NaI(Tl) (SuN) calorimeter. The ^{60}Zn nucleus was populated through β^+-decay of ^{60}Ga. The resulting spectra were analyzed using the Total Absorption Spectroscopy technique. Total absorption spectroscopy was used to determine the β feeding intensity up to 10 MeV and compared with Shell Model and Quasi-particle Random Phase Approximation calculations. The experimental data was also used in the newly developed β^+ Oslo method, an extension of the β Oslo method for proton-rich nuclei. This thesis presents a discussion on the first application of the β^+ Oslo method.

Additionally, this thesis describes a Bayesian inference code used to constrain the parameter

space of models used to calculate the relevant cross section. This tool provided a statistically rigorous uncertainty quantification on the nuclear level density and γ-ray strength function extracted from the β^+ Oslo method. These uncertainties were incorporated into the final cross section and reaction rate calculations performed in the TALYS nuclear reaction code. The experimentally determined $^{59}Cu(p,\gamma)^{60}Zn$ cross section implies that the reaction flow of both astrophysical processes are dominated by capture to heavier masses with only a small amount entering the NiCu cycle in the relevant temperature ranges.

TABLE OF CONTENTS

CHAPTER 1

INTRODUCTION

Throughout its history, humanity has striven to answer the question: Where do we come from? One method to resolve this inquiry, is to understand what we are made of. We began by searching within ourselves and our surroundings. Through generations of careful study, we realized that everything within and outwith ourselves is comprised of atoms: oxygen and nitrogen in the air that fills our lungs, carbon in all creatures that populate the world, the numerous metals in our tools and architecture. Therefore, to understand our own origin we must comprehend the origin of the elements that comprise our universe.

In the past century, great strides have been made in our knowledge of atoms and their formation. The atomic nucleus discovered in 1911 by Rutherford[1], the first proposal that the sun plays a role in creating elements beyond hydrogen in 1920 by Eddington [2], and Eddington's student Lemaî tre founding the big bang theory in 1931[3]. In the subsequent decades, researchers in both nuclear physics and astrophysics continued to make discoveries in their respective fields. In 1957, Margret and Geoffrey Burbidge, William Fowler, and Fred Hoyle compiled knowledge from both fields in their review article "Synthesis of the Elements in Stars"[4]. This groundbreaking article not only explained how stars form heavier elements out of lighter ones through nuclear fusion; but, also proposed three major processes that form the most heavy elements when stars die. They proposed that heavy element nucleosynthesis occurs with either the slow (s), rapid (r), or proton (p) processes. The s and r processes arise in neutron dense environments, with the s-process creating elements up to lead and bismuth, and the r-process accessing masses from iron and past uranium. The p-process proposed in this work suggested a proton rich environment, where mass is gained through proton captures. This view has since been disproven, replaced with a path that moves toward lighter nuclei through photodisintegration reactions[5]. This publication illustrated that answering the question "Where do we come from?" required a multidisciplinary field that combines nuclear physics, astronomy, and astrophysics, now known as Nuclear Astrophysics.

Since this publication, many more nucleosynthesis processes have been discovered beyond those initial three. This work focuses on the rp-process, occurring in Type I X-Ray Bursts, and the νp process, found in the proton rich nuetrino driven winds of core collapse supernovae. Both of these processes have an uncertain step: when the ^{59}Cu nucleus captures a proton to become ^{60}Zn, is it more likely to create heavier isotopes or decay to a lighter mass, entering the NiCu cycle? Answers to this question, can be found by studying the statistical properties ^{60}Zn. Through improving our understanding of the structure of this isotope, we were able be able to better determine which path each process takes.

This thesis begins with a discussion on relevant astrophysical topics and nuclear properties. Afterwards, the experimental setup and procedures are detailed followed by a description of the data analysis tools used and developed. Next, an examination of the results in comparison to theorectical predictions and other measurements is given; concluding with the impact of these results on the rp and νp processes.

CHAPTER 2

NUCLEAR BACKGROUND

If one were to zoom in on an atom, they would first encounter a cloud of negatively charged leptons, typically electrons. After passing through this cloud there would be a large volume of empty space and at the center one would find the nucleus. The nucleus is the core of the atom, is comprised of protons and neutrons, has a net positive charge. A nucleus is defined by its mass number A, its proton number Z, and the number of neutrons N = A - Z. Elements are defined as nuclei with unique Z values and isotopes are nuclei with the same Z but different N values. While elements are depicted on the periodic table they are organized only with Z. Representing isotopes requires a different approach, showing how each Z can be combined with multiple N. This representation is called the chart of nuclides shown in Fig. 2.1. Z is displayed on the vertical axis and N is on the horizontal axis. The black squares are the stable isotopes, those that will never decay and are naturally found in environments like the solar system. This stretch of stable isotopes is also called the valley of stability and outside of the valley, radioactive nuclei are found. Radioactive nuclei undergo a decay process, releasing energy and changing form to become an isotope closer to the center of the valley. Below the valley exist neutron rich isotopes and above the valley are the proton rich (neutron deficient) isotopes.The columns and rows outlined in black represent values of Z and N known as magic numbers. These values are special in that nuclei in these spaces are more stable than their counterparts outside. These values are explored and explained using the Nuclear Shell Model 2.5.1, a theoretical model based on atomic electron shell model, developed for protons and neutrons within the nucleus

This chapter will provide a brief overview on reaction basics, γ-ray transition and β-decays. In addition to discussing the Shell Model, there is a description of the Quasi-particle Random Phase Approximation. Both of these models were compared to the experimental results of the present thesis. There are also several mentions of the TALYS [6] nuclear reaction code that uses Hauser-Fesback(Sec. 2.5.3) calculations to predict reaction cross sections(Sec. 2.2.2).

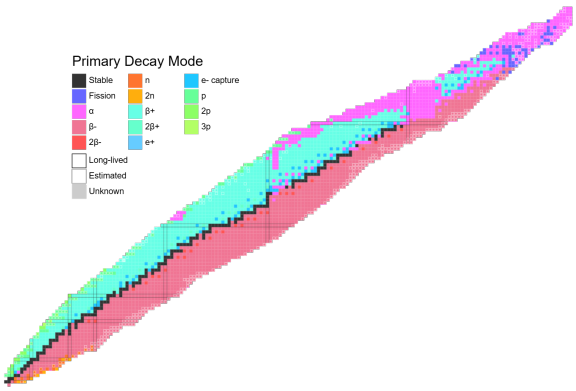

Figure 2.1 The Chart of Nuclides. The various colors correspond to the primary decay mode the isotope undergoes to reach stability.

2.1 Binding Energy and Separation Energies

The mass of the nucleus m_i more than the sum of Z and N but also includes the energy of the strong force holding it together known as the binding energy B. The binding energy is a function of both Z and N and can be thought of as a competition between the strong force holding all of the baryons together and the electromagnetic force attempting to push the protons apart. Thus the binding energy can also be described as the amount of energy needed to separate all of the nucleons that make up the nucleus. The binding energy is written as $B(Z,N) = \Delta mc^2 = (Zm_p + Nm_n - m_i)c^2$, where Δm is the difference between m_i and A, known as the mass excess. Using this concept, it is also possible to describe the energy needed to separate only one nucleon from the nucleus with a term called separation energy. The proton separation energy S_p is the binding energy difference between ${}^{A}_{Z}X$ and ${}^{A-1}_{Z-1}X$:

$$S_p = B(Z,N) - B(Z-1,N)$$

and the neutron separation energy S_n is the difference between ${}^{A}_{Z}X_N$ and ${}^{A-1}_{Z}X_{N-1}$:

$$S_n = B(Z,N) - B(Z,N-1)$$

2.2 Reactions

Nuclei can change into different isotopes or elements by emitting or capturing another particle. An isotope can be represented as ${}^{A}_{Z}X_N$ or simplified as ${}^{A}X$, where X is the symbol for the element

corresponding to Z. A two body nuclear reaction can be described as

$$^{A}X + a = {}^{B}Y + b$$

or $X(a, b)Y$ with a and b as absorbed and emitted particles (baryons or nuclei) respectively and Y as the resultant isotope. The left hand side represents the entrance channel and the right hand side shows the exit channel. In calculations, a channel needs to conserve the set of quantum numbers (spin,orbital angular momentum, total spin,etc.) that correspond to the particles in question. Every nuclear transmutation must follow a set of conservation laws:

- Energy - all the energy $m_x c^2 + m_a c^2 + E_x + E_a$ must be distributed among the reaction products as $m_Y c^2 + m_b c^2 + E_Y + E_b$
- Linear Momentum - determines the angles at which the reaction products are emitted.
- Angular Momentum - the total angular momentum of all reactants must be the same as that of all products.
- Parity - the behavior under one spacial reflection must be the same before and after the reaction
- Charge - total charge must remain the same before and after the reaction
- Baryon Number - the total number of protons and neutrons must be the same on both sides
- Lepton Number - for every lepton (e.g. $e^{\pm}, \nu_e, \tilde{\nu}_e$) involved in the reaction an equal number must exists as a product. Matter gives a value of +1 and antimatter counts as -1.

This thesis focuses on a particular type of reaction, known as radiative capture. In these processes the isotope X captures a baryon and the new Y isotope emits γ-rays.

2.2.1 Q Value

The Q value describes the amount of energy a system has available for a reaction to occur. It is defined as the difference in rest mass energy before and after the reaction [7]. In the case of the

two body example:

$$Q = (m_i - m_f)c^2 = m_X c^2 + m_a c^2 - m_Y c^2 - m_b c^2$$

A process with a positive Q value releases energy when it occurs and a negative Q values requires energy to occur.

2.2.2 Cross Section

A reaction cross section, is the probability that a reaction will occur and can be simply described as number of successes over opportunities. Assume there is a beam of particles of type a at a rate of R_a incident on a target of material X that has N_X particles per unit area. A nearby detector at angle ϕ with respect to the beam axis covers a solid angle of $d\Omega$ and measures products at a rate of R_p. The cross section σ of this reaction can then be described as [7]:

$$\sigma = \frac{(rate\ of\ product\ detection)}{(rate\ of\ beam\ particles)(number\ of\ X\ nuclei\ in\ area)} = \frac{R_p}{R_a\ N_X}$$

Since the detector can only measure within its $d\Omega$ coverage angle, it is reasonable to say that not all products b were detected. Therefore, the description above is a partial cross section. The total cross section would be the partial cross section integrated over a spherical shell around the reaction location:

$$\sigma_{tot} = \int \frac{d\sigma}{d\Omega} d\Omega = \int_0^{\pi} sin\theta d\theta \int_0^{2\pi} \frac{d\sigma}{d\Omega} d\phi$$

To know the cross section for a specific reaction (e.g X(a,b)Y), one would calculate the detection rate of b type particles R_b and substitute that for R_p. With this information, the cross section of the reverse reaction Y(b,a)X can also be calculated with the reciprocity theorem:

$$\frac{\sigma_{Y \to X}}{\sigma_{X \to Y}} = \frac{(2j_X + 1)(2j_a + 1)k_{Xa}^2(1 + \delta_{Yb})}{(2j_Y + 1)(2j_b + 1)k_{Yb}^2(1 + \delta_{Xa})}$$

where k is the wave number, j is spin, and the factor $(1 + \delta_{ij})$ doubles the cross section for identical reactants.

Now consider a situation where some particle a impinges on a single nucleus of element X. The particle can interact elastically (scattering), where the interaction conserves kinetic energy and the

particle leaves just as it came, or inelastically (reaction), where the particle and target change due to their interaction (e.g. energy transfer (p,p'), capture (p,γ),etc.). The total cross sections for these conditions are given by:

$$\sigma_{scatter} = \frac{4\pi}{k^2}(2l+1)sin^2\delta_l$$

$$\sigma_{reaction} = \frac{\pi}{k^2}(2l+1)(1-|e^{2i\delta_l}|^2)$$

where l is the orbital angular momentum and δ_l is the corresponding phase shift. The phase shift is an energy dependent factor, and certain energies can cause sharp oscillations in the cross section. These oscillations, called resonances, signify a maximum likelihood for the incident particle to exist within the volume of the target nucleus. In the resonant view, the reaction cross section can be described with the Bright-Wigner formula [7]:

$$\sigma_{reaction}(E) = \frac{(2l+1)\pi}{k^2}\frac{\Gamma_{\lambda e}\Gamma_{\lambda_r}}{(E-E_\lambda)^2+\Gamma_\lambda^2/4}$$

where Γ_λ is the total resonance width, which is the full width at half maximum of the resonance peak λ. $\Gamma_{\lambda e}$ and Γ_{λ_r} are the partial widths of the entrance and reaction channels respectively.

2.3 γ-ray Transitions

γ-ray transitions occur when a nucleus in an excited state, emits γ-rays to access its ground state or when a nucleus is energized to an excited state by a γ-ray. The transition mode is categorized into two groups; electric (E) and magnetic (M) transitions. These groups are further separated by their multipolarity, which corresponds to the angular momentum L the γ-ray has when it is emitted during the transition. EL and ML transitions differ in that EL follow the rule $(-1)^L$ and ML transitions use $(-1)^{L+1}$. E transitions are always more likely to occur than M for the same L and higher values of L are less probable than lower values.

2.4 β-Decay

Another nuclear transmutation process is β-decay, which changes a radioactive isotope into another more stable isotope. This process conserves mass number A but, shifts proton number Z

Table 2.1 Table of β-decay selection rules.

Transition	L	ΔJ	$\Delta\pi$
Fermi	0	0	0
Gamow-Teller	0	0,1	0
1^{st} Forbidden	1	0,1,2	1
2^{nd} Forbidden	2	1,2,3	0
3^{rd} Forbidden	3	2,3,4	1

and neutron number N by 1. In a β-decay a nucleon (p/n) transforms into the other type by emitting a positron/electron and a neutrino/anti-neutrino. For a neutron the decay process is: $n \rightarrow p + e^- + \bar{\nu}_e$ which occurs in ≈ 10.2 minutes [7]. A proton's β^+-decay process is: $p \rightarrow n + e^+ + \nu_e$ A proton does not decay naturally in isolation like single neutrons do. However, in sufficiently neutron deficient isotopes (e.g. ^{60}Ga), it is an allowed method to achieve a more stable configuration. Protons can also capture electrons to become neutrons in the electron capture process as: $p + e^- \rightarrow n + \nu_e$.

The β-decay half life is given by

$$t_{1/2} = \frac{\kappa}{f_0(B_F + B_{GT})}$$

where κ is a constant equal to 6147 s, f_0 is a phase space integral (Fermi Integral) describing lepton kinematics, and B_F and B_{GT} are reduced transition probabilities of the Fermi and Gamow-Teller (Sec. 2.4.2) transition types.

β-decays obey the transition rules, $\Delta J = |J_f - J_i|$ [8]; $\pi = (-1)^L$ which determine the excited states that the compound nucleus is likely to occupy. The most probable decay types are known as allowed transitions of which there are two: Fermi and Gamow-Teller. A Fermi transition does not change spin or parity when transmuting to the compound nucleus. This includes transitions from isobaric analogue states, where the ground state of the parent nucleus has the same $J\pi$ and similar structure as an excited state in the child. The first five transition types are tabulated in Table.2.1. The transition probabilities can also be described by their $log(ft)$ value. Rearranging the half-life equation above

$$ft_{1/2} = \frac{\kappa}{B_F + B_{GT}}$$

gives the ft value that is purely based on the structure of the nuclei. Due to their typically large

values, the log of ft is used. Transitions with lower log(ft) are more probable with values between 2.9 - 3.3 considered as allowed transitions [8].

2.4.1 Weak force

The weak force manages β-decays through the $W^{\pm}$ and Z bosons. These bosons have a large mass of $m_{W^{\pm}} \approx 80.37 MeV/c^2$ $m_Z \approx 91.12 MeV/c^2$ leading to their incredibly short lifetime $\tau_{W^{\pm},Z} \approx 10^{-24}$ [9]. The weak force has two coupling constants: the axial-vector constant g_A and the vector constant g_V. g_A is related to nuclear spin [10]. These constants are typically quoted as the ratio $g_A/g_V = g_A \approx -1.27^{+0:00409}_{-0:00445}$ [10] and $g_V = 1$ under the assumption of conserved vector current [11]. This ratio represents the strength of the weak interaction and these constants appear in the calculation of the Gamow-Teller reduced transition probability (Sec. 2.4.2) from the β-decay Feeding Intensity (I_β Sec. 2.4.3) as well as the operators for Fermi and Gamow-Teller.

2.4.2 Fermi and Gamow-Teller Reduced Transition Probability (B_F & B_{GT})

The reduced Fermi transition probability B_F is defined as:

$$B_F \equiv \frac{g_V^2}{2J_i + 1}|M_F|^2$$

with M_F is the Fermi nuclear matrix element [8].

The Gamow-Teller Reduced Transition Probability B_{GT} is defined [8] as:

$$B_{GT} \equiv \frac{g_A^2}{2J_i + 1}|M_{GT}|^2$$

where M_{GT} is the Gamow-Teller nuclear matrix element calculated from the Gamow-Teller operator $\hat{O}$, a combination of the Pauli spin operator σ_p and the isospin operator τ which handles weak interactions [12]

$$M_{GT} = \langle f||\hat{O}||0\rangle = \langle f||\sigma_p\tau||0\rangle$$

B_{GT} represents the Gamow-Teller transition probability from the ground state of the parent nucleus to an excited state in the child nucleus with the same parity and a spin difference no greater than 1.

2.4.3 β-decay Feeding Intensity (I_β)

β-decay Feeding Intensity (I_β) describes the probability a specific state is populated through β-decay. It is the ratio of the β-decay rate to one state λ_f over the total β-decay rate λ. The total

decay rate λ is

$$\lambda = \frac{1}{\tau_{1/2,GT}} = \frac{1}{\kappa}\sum_f [g_v^2 B_{F,f} + g_A^2 B_{GT,f}] f(Q_f)$$

and λ_f is an individual component of the sum in λ. Therefore the β feeding intensity is

$$I_\beta = \frac{\lambda_f}{\lambda}$$

I_β can be determined experimentally using the Total Absorption Spectroscopy Method detailed in Sec. 5.2

2.5 Theoretical Frameworks

There exists a plethora of framework used to describe the various properties and behaviors of nuclei. This section presents a high level discussion on three such methods used for this work: The Nuclear shell Model which describes structure, the Quasiparticle Random Phase Approximate that describes nuclear excitation, and the Hauser Feshback formalism for deducing reaction cross sections.

2.5.1 Nuclear Shell Model

The Nuclear Shell Model aims to describe the structure of the atomic nucleus by defining the quantum state of each nucleon in a mean field while accounting for the Pauli exclusion principle [13]. In the shell model, the Hamiltonian is separated into two parts, a model component H_0 that describes how the nucleons are organized and a residual interaction component B that describes how the nucleons behave with respect to one another

$$H = H_0 + B$$
$$H_0 = \sum_i^A h_0(i) = \sum_i^A [t(i) + v_0(i)]$$
$$B = \sum_{i<j=1}^A v(i,j) - \sum_i^A v_o(i)$$

Here, A is the mass number (total number of nucleons), t(i) is the kinetic energy operator on nucleon i, v_0 is the shell model potential (e.g. Harmonic Oscillator, Woods-Saxon), and v(i,j) represents the many body potential caused by nucleon interactions [14].

With this framework, the shell model specifies wavefunctions for each state in a nucleus. It also finds energy eigenvalues for each nucleon. These eigenvalues are typically close in energy; however, every so often a large increase occurs from one value to the next. The nucleon number preceding the energy jump is known as a magic number and signifies a particularly stable configuration, since it takes a lot of energy to reach the next mass number. Nuclei with a magic number of protons and/or neutrons have a higher binding energy than their neighbors and longer life time, if radioactive. The mathematical description above only agrees with experimental measurement up to the third magic number. In order to improve agreement, the spin-orbit coupling term $v_{l\cdot s}(i)$ is added to the potential

$$H_0 = \sum_{i}^{A}[t(i) + v_0(i) + v_{l\cdot s}]$$

This term represents an assumption that interaction between any two nucleons effectively creates a spherical potential [15].

The shell model also predicts isobaric analogue states (IAS); states in different nuclei with the same A and same structure but different composition of nucleons. IAS appear at similar relative energies. These states are special in that their similarity permits superallowed Fermi transitions. The IAS wavefunction |IAS> is defined as [12]:

$$|IAS >= \frac{1}{2\sqrt{N-Z}} \sum_{j=1}^{A} \tau_{-}(j)|\Psi_0 >$$

where $|\Psi_0 >$ refers to the ground state and $\tau_{+}(j)$ is the isospin raising operator which changes a proton into a neutron while conserving its spacial wave function. Shell Model calculations used in this thesis were performed by Dr. B. Alex Brown and used to compare with the experimental I_β(Sec. 5.4.

2.5.2 Quasi Particle Random Phase Approximation (QRPA)

The Random Phase Approximation (RPA) method correlates the ground and excited nuclear states. It views nuclear excitation as the creation of a particle hole (p-h) pair, where the particle exists at some higher energy state v and the hole occupies the original position of the particle . One derivation operates under the quasi-boson assumption, which treats a pair of fermions (e.g. p-h pair) as a collective boson (phonon) excitation, neglecting the commutation relationship for boson

field operators [16]. RPA also assumes the ground state nucleus is sufficiently described with a static mean field such as Hartree-Fock-Bogoliubov (HFB) [17]. Extending RPA to Quasi Particle RPA (QRPA) means the degrees of freedom of two single particles are treated as quasi-bosons. QRPA uses the ansatz for the phonon creation operator [16] :

$$Q_v^\dagger = \frac{1}{2}\Sigma_{kk'}(X^v_{kk'}\alpha^\dagger_k\alpha^\dagger_{k'} - Y^v_{kk'}\alpha_k\alpha_{k'})$$

where $\alpha^{(\dagger)}$ is the creation (destruction) operator for the quasi-particle pair, k<k' are all particle hole pairs, the elements of matrices X and Y are amplitudes of the two quasi-particle component k,k'. X describes how much each pair contributes to the collective excitation and Y corrects for correlated components in the ground state. With this ansatz, the QRPA equation is

$$\begin{pmatrix} A & B \\ -B & -A \end{pmatrix}\begin{pmatrix} X \\ Y \end{pmatrix} = E_v \begin{pmatrix} 1 & 0 \\ 0 & -1 \end{pmatrix}\begin{pmatrix} X \\ Y \end{pmatrix}$$

where E_v is the excitation energy of state v, A and B are matrices related to the matrix elements of pp, hh, and ph contributions [16]. The solutions of the X and Y matrices are of particular importance in calculating the Gamow-Teller transition strengths of β-decays in astrophysical environments.

From a QRPA approach, the matrix element M_{GT} can be calculated as:

$$M_{GT} = \langle 0|[Q_v, \sigma_p\tau]|0\rangle$$

where Q_v is the phonon destruction operator, the conjugate transpose of the $Q_v^\dagger$ ansatz in Sec. 2.5.2.

2.5.3 Hauser Feshback

The Hauser - Feshback (HF) theory aims to calculate differential cross sections over energy by describing the formation and decay of a compound nucleus. For a two body reaction:

$$^AX + a \rightarrow {}^DC^* \rightarrow {}^BY + b$$

where the left and right sides are the entrance and exit channel as in Sec. **??**, and the $^DC^*$ is the compound nucleus with mass D. HF theory relies on the assumptions

- The compound nucleus is created at a highly excited energy level Ex, where there are many ($\geq$ 10 [18]) states in the excitation energy bin

- The phases of the wave functions for these levels are random; therefore, all interference terms cancel when averaged
- The exit channels are determined only by the statistical properties of the nucleus, independent to the formation [19].

The capture cross section is given by

$$\sigma^{\mu\nu}(E_{ij}) = \frac{\pi\bar{h}/(2\mu_{ij}E_{ij})}{(2J_i^\mu+1)(2J_j^\mu+1)}\Sigma_{J,\pi}(2J+1)\times\frac{T_J^\mu(E,J,\pi,E_i^\mu,J_i^\mu,\pi_i^\mu)T_o^\nu(E,J,\pi,E_m^\nu,J_m^\nu,\pi_m^\nu)}{T_{tot}(E,J,\pi)}$$

where $\sigma^{\mu\nu}$ is the cross section of the reaction $i^\mu(j,o)m^\nu$, E_{ij} the center of mass energy, μ_{ij} is the reduced mass. J, E, and π are the spin, excitation energy, and parity of the state respectively. Without subscripts these variables refer to the compound nucleus, superscripts represent excited states, and subscripts denote the states of the initial and final nuclei. The total transmission coefficient $T_{tot} = \Sigma_{\nu,o}T_o^\nu$ sums over coefficients from all states within the energetically allowed exit channels [20]. The total transmission coefficient of the exit channel T_o^ν in the case of γ-ray emission is

$$T_\gamma(E,J,\pi) = \Sigma_{\nu=0}^{\nu_m}T_\gamma^\nu(E,J,\pi,E_m^\nu,J_m^\nu,\pi_m^\nu) + \int_{E_m^{\nu_m}}^{E}\sum_{J_m,\pi_m}T_\gamma(E,J,\pi,E_m,J_m,\pi_m)\times \rho(E_m,J_m,\pi_m)dE_m$$

The first sum is over the transmission coefficients for the experimentally separable states at lower energies, also called the discreet region. Despite the assumption that the compound nucleus is populated in the continuum, it is still important to include the discreet states in the calculation because there can be γ transitions from the continuum to discreet levels. Within the integral, the terms refer to the level density of states (NLD) ρ (Sec. 2.5.3.2) and transmission coefficients (Sec. 2.5.3.3) at energies where levels are not yet separable, known as the continuum region. The transmission coefficients of the entrance channel can be calculated with an Optical Model potential (OMP) (Sec. 2.5.3.1). The NLD and T_γ are extracted in the Oslo Method described in Sec. 6.1.

2.5.3.1 Optical Model Potentials (OMP)

Optical Model Potentials (OMP) represent nucleon - nucleus interactions in a manner analogous to light interacting with a medium in optics. They have a real component that describes scattering or emission of a particle and an imaginary component that explains absorption. The imaginary absorption component relies on the transmission coefficients of the initial and final states [20]. The phenomenological OMPs used in the TALYS HF calculations are the local and global parameterizations by Konning and Delaroche (KD) [21] and a semi-microscopic model can also be with Juekenne, Lejeune, and Mahaux (JLM) calculations [22]. The KD model is based on a phenomenological OMP U of the form

$$U(r,E) = -R_V(r,E) - iI_V(r,E) - iI_D(r,E) + R_{SO}.1.\sigma + iI_{SO}.1.\sigma + R_C(r)$$

where R and I refer to the real and imaginary components. The subscripts V, D, and SO are the volume, surface, and spin-orbit potentials respectively. E is the energy in the laboratory frame in MeV. JLM based on the Breukerner-Hartree-Fock approximation [22]. Low energy interactions between a charged nucleon and the nucleus are largely mediated by the Coulomb interaction, hindering capture attempts leading to a very low capture cross section at energies under the Coulomb barrier [23]. Therfore measureing cross sections at low energies is challenging.

2.5.3.2 Nuclear Level Density (NLD)

The Nuclear Level Density (NLD), symbolized as ρ, describes how many levels there are per unit energy. It is the function $\rho(E,J,\pi) = \frac{\Delta N(E,J,\pi)}{\Delta Ex}$, where ΔN is the number of available levels, and ΔE_x is the excitation energy bin. The total level density is then $\rho_{tot} = \sum_{J,\pi} \rho(E,J,\pi)$. It is assumed that the spin and parity can be isolated into separate functions as $\rho(Ex,J,\pi) = \rho(Ex)g(Ex,J)F(Ex,\pi)$, where g and F are the spin and parity distributions respectively.

The many available spin distribution models in the literature (e.g [24]) depend on a spin cutoff parameter σ. σ is typically a function of A and Ex; not to be confused with $\sigma_{\mu\nu}$ the cross section. There is often a σ^2 term in the denominator of these equations that can be understood as the moment of inertia that comes from the spin distribution [24]. Several theoretical spin cutoff models are

described in [25]. The rigid sphere model used in the present analysis is:

$$\sigma^2 = 0.0145 A^{5/3} \sqrt{E_x/a}$$

where a is a parameter related to orbital energy spacing. More information on derivation of this equation can be found in [26].

Parity distributions often assume there are an equal number of positive and negative states [24]. For nuclei with few available levels, such as those near the drip lines, parity asymmetry can be a relevant factor [18]. There are models that include asymmetric parity such as [27] with a phenomenological approach as well as microscopic and semi-microscopic methods by Goriely et al. [28] used in TALYS [6] calculations. The most commonly used NLD models are the Constant Temperature Model (CT) and the Back Shifted Fermi Gas Model (BSFG) which are described in Sec. 5.2.1. The semi-microscopic models can be adjusted with the parameters$a$ and δ. a adjusts the slope and can be thought of as the level density parameter discussed in Sec. 6.1.4. δ controls the energy offset. These parameters are applied to the semi-microscopic models with the equation [29]:

$$\rho(E_x, J, \pi) = exp(a\sqrt{E_x - \delta})\ \rho_{micro}(E_x - \delta, J, \pi)$$

Table 2.2 Available NLD models in TALYS[6].

Keyword	Model	Ref.
ldmodel 1	Constant Temperature & Fermi Gas Model	[30]
ldmodel 2	Back-shifted Fermi Gas Model	[31]
ldmodel 3	Generalised Superfluid Model	[32, 33]
ldmodel 4	Skyrme-Hartree-Fock-Bogolyubov level densities from numerical tables	[34]
ldmodel 5	Skyrme-Hartree-Fock-Bogolyubov combinatorial level densities from numerical tables	[35]
ldmodel 6	Temperature-dependent Gogny-Hartree-Fock-Bogolyubov combinatorial level densities from numerical tables	[36]

2.5.3.3 γ-ray Strength Function (γSF)

The γ-ray Strength Function (γSF) describes the average probability of a γ-ray of a particular energy to emitted or absorbed from a nucleus as a function of γ-ray energy. The γSF can be discussed

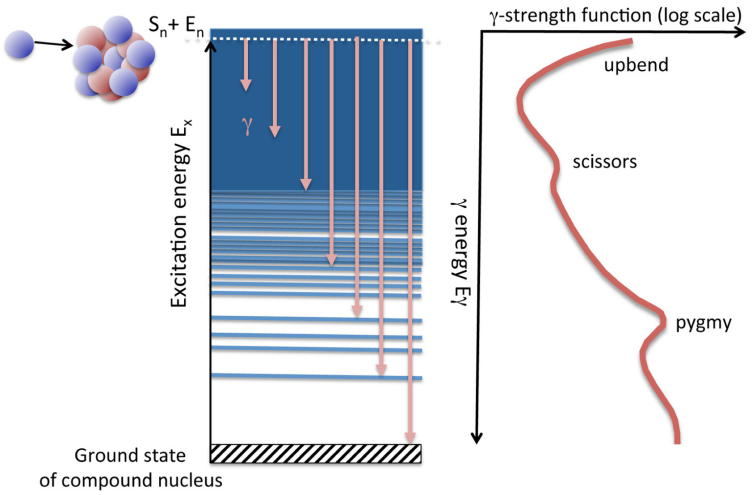

Figure 2.2 The γSF as it relates to energy from γ-ray de-excitation [18]. Transitions from states close in energy correspond with upbend and scissor features while those with large energy differences relate to the pygmy and GDR (not shown).

as having separate upward (excitation) $\overrightarrow{f_{XL}}$ and downward (de-excitation) $\overleftarrow{f_{XL}}$ functions. However, under the Brink-Axel hypothesis, the upward and downward functions are said to be approximately equal $f_{XL} = \overrightarrow{f_{XL}} = \overleftarrow{f_{XL}}$. The hypothesis also states that the function f_{XL} only depends on the γ-ray's energy, not the energies, spins or parities of the initial and final states [37, 38].

The γSF is directly related to the γ-ray transmission coefficient T_γ by:

$$T_{XL}(E_\gamma) = 2\pi E_\gamma^{2L+1} f_{XL}(E_\gamma)$$

$$f_{XL}(E_\gamma) = E_\gamma^{-(2L+1)} \langle \Gamma_{XL}(E_\gamma) \rangle / D$$

where T_{XL} is the transmission coefficient of E or M type transition with multipolarity L, $f_{XL}(E_\gamma)$ is the γSF, $\langle \Gamma_{XL} \rangle$ is the average radiative width, D is the resonance spacing and E_γ is the energy of the γ-ray [39]. In the context of cross section calculations in astrophysical environments, the most important XL are the dipole (E1 & M1) components of the γSF. There are several models to describe these, some of which are described in Tab. 2.3.

E1 models are typically Lorentzian based with energy dependent widths and finite values at zero energy to accurately describe the shape of the giant dipole resonance (GDR), which appears at $E_\gamma \approx 10 - 15$ MeV [39]. The GDR is said to result from the collective oscillation of protons within the nucleus and appears as a wide peak of high probability . E1 can also have a double

Table 2.3 The available models for the γSF in TALYS [6].

Keyword	Transition	Model	Ref.
`strength 1`	$E1$	Kopecky-Uhl Generalized Lorentzian	[40]
`strength 2`	$E1$	Brink-Axel Standard Lorentzian	[41, 42]
`strength 3`	$E1$	Skyrme-Hartree-Fock BCS model with QRPA	[43]
`strength 4`	$E1$	Skyrme-Hartree-Fock-Bogoliubov model with QRPA	[44]
`strength 5`	$E1$	Hybrid model (Lorentzian model with energy and temperature dependent width)	[45]
`strength 6`	$E1$	Temperature-dependent Skyrme-Hartree-Fock-Bogoliubov model with QRPA	[44]
`strength 7`	$E1$	Temperature-dependent Relativistic Mean Field Model	[46]
`strength 8`	$E1$	Gogny-Hartree-Fock-Bogoliubov model with QRPA by based on the D1M version of the Gogny force	[47]
`strength 9`	$E1$	Simplified Modified Lorentzian Model	[48]
`strength 10`	$E1$	Simplified Modified Lorentzian Model	[**?**]
`strengthM1 1`	$M1$	Standard Lorentzian Model as parameterized in RIPL3 Library	[49]
`strengthM1 2`	$M1$	$M1$ normalized on $E1$ as $f_{E1}/(0.0588A^{0.878})$	
`strengthM1 3`	$M1$	Addition of spin-flip and scissors mode	[50, 51, 52]
`upbend y/n`	$M1$	Flag to include upbend or not	[53, 54, 55, 56]

peak structure in this range, whose max values are related to the nucleus' deformation away from a spherical shape. In this case oscillations occur along both a major and minor axis.

The E1 model used in this work is the Skyrme-Hartree-Fock-Bogoliubov with QRPA detailed in [17].Within TALYS all E1 models can be adjusted with parameters `Etable`, `ftable`, `wtable`. Etable is the centroid of the GDR, wtable is its FWHM, and ftable applies a non-physical scaling. These parameters are applied with the equation

$$F_{E1}^{adjusted}(E_\gamma) = f_{table} F_{E1}^{original}(E_{E1} + w_{table}(E_\gamma - E_{E1}) + E_{table})$$

where F is the γSF and E_{E1} is the energy at the middle of the γSF [29].

M1 models also have a Lorentzian shape but with smaller peak height compared to the GDR. These models describe the scissors and spin-flip features of the γSF. The scissors mode is a collective motion effect of nucleons in a deformed nucleus [57]. For more spherically shaped nuclei, there is a unique increase in the γSF at low energies [58]. This is known as the low energy

enhancement or upbend, and has been shown to result from M1 transitions [59]. The M1 low energy enhancement is adjusted with `updende`, `upbendc`, `upbendf`, and `beta2`. upbende is an energy dependent factor, beta2 describes the deformation of the isotope, while upbendc and upbendf are normalization terms. These parameters shape the upbend with

$$M_{up}(E) = C\ exp(-F * |\beta^2|)\ exp(-\eta * E)$$

where C is upbendc, F is upbendf, β^2 is beta2, η is upbende, and E is the γ energy.

CHAPTER 3

ASTROPHYSICAL BACKGROUND

The previous chapter discussed the structure of nuclei, how they can change (reactions/decays), and models that describe these transmutations. This chapter will reference these ideas to explain the formation of nuclei in the universe. It begins by describing how the lightest nuclei were formed in the Big Bang, then discusses nucleosynthesis during stellar evolution. It finishes with sections reviewing the multiple nucleosythesis processes for elements more massive than Iron, with a focus on the rp and νp processes which contain the $^{59}Cu(p,\gamma)^{60}Zn$ reaction, which is the focus of the present thesis.

3.1 Big Bang Nucleosynthesis (BBN)

At $\approx$ 0.1 s after the Big Bang, the average temperature was 3e10 K with a mean photon energy E $\approx$ $10MeV$ [60]. Since the photon energy was about 10 times higher than the rest energy of electron positron pairs (1.022 MeV), pair production and annihilation were in equilibrium. There was also an equilibrium in baryonic matter as neutrinos were still strongly coupled to them through the weak force, so protons and neutrons could freely convert back and forth [60].

Around 6s after the Big Bang, the temperature was 500 keV, lower than the rest mass of electrons and positrons and annihilation of these anti particles begins [61]. Therefore, the universe has cooled to a point where the baryon equilibrium no longer holds as the weak force interaction weakens, reducing the neutrino capture rate for baryons. As time passes, free neutrons decay into $p + e^- + \bar{\nu_e}$, and baryon matter becomes dominated by protons [60]. The ratio of protons to neutrons is effectively "frozen" until $t_{universe} \approx t_{nuetron}$, fixing the ratio to about 1 neutron for every 7 protons [62]. Big Bang nucleosynthesis (BBN) begins with the creation of the first nuclei after the proton - neutron freeze out, when the average temperature of the universe dropped below $\approx$ 0.7 MeV [62].

BBN ends $\approx$ 1000s after the Big Bang at temperature around 3×10^8 K [60]. The majority of

baryon matter is now either free protons or ^4He nuclei. This results in initial abundances of ≈ 0.75 H, $.245 \pm 0.003$ ^4He, and $\leq 10^{-9}$ Li [9]. ^7Be after BBN becomes ^7Li after electron capture.

3.2 Stellar Nucleosynthesis

After BBN and the formation of galactic clouds, the Hydrogen and Helium plasma further condensed into what are known as protostars. As they contract under their own gravitation, the temperature and pressure increases. With enough mass, the temperature will exceed 10^6 K, igniting the hydrogen fusion process, and turning the protostar into a full main sequence star [63]. Main sequence stars fuse lighter mass nuclei into heavier mass products through their high temperatures generated from compression under their gravity. Once the material with the lowest Coulomb barrier has been used, reactions will slow, reducing the outward pressure that stabilizes the star [7]. Without the added pressure, the star contracts, causing its temperature to increase until it is high enough for the fuel with the next lowest barrier to begin fusion. The star is again stable against contraction and this process repeats until there is either no more fuel or an iron core is formed. Depending on the star's mass, it can fuse material in some or all of the stages listed in the following sections. As heavier material is formed in the core, the elemental abundance stratifies into the onion like formation depicted in Fig. 3.1. These stellar fusion processes are thoroughly investigated in *Nuclear Physics of Stars* by Christain Illiadis [7]. Here, an overview is presented.

3.2.1 Hydrogen fusion

Being a main sequence star means that the core temperature is high enough for hydrogen fusion. Stars spend the majority of their life in this hydrogen burning phase. Hydrogen fusion occurs one of two ways depending on when the star was formed. The oldest stars formed from nearly pure Hydrogen clouds and must fuse Hydrogen using the pp-chains, forming Helium from four Hydrogen atoms. Now, stars can form from clouds with a mixture of pre-existing elements and fuse through either the pp-chains or the CNO cycle. Both H fusion processes are described below.

3.2.1.1 The pp-chains

The pp-chains are three processes that fuse Hydrogen into ^4He [7]. These chains all begin with 2 protons fusing into a deuteron. This first step takes an average of 9×10^9 yr. Once the deuteron

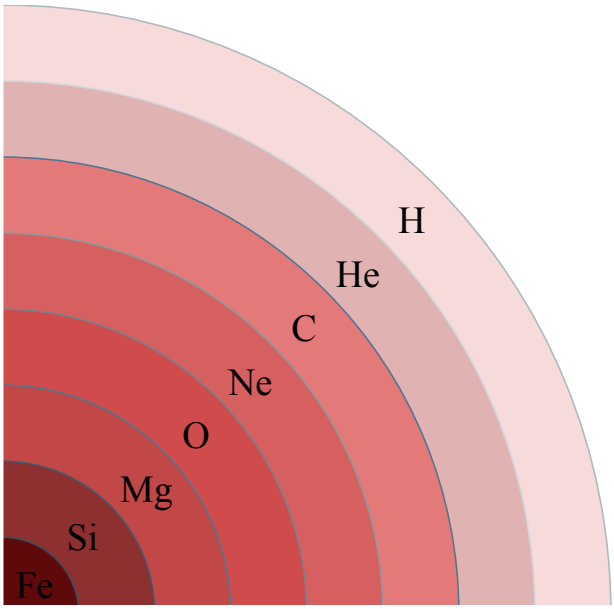

Figure 3.1 Layered structure of a massive star. As a new heavy core forms during burning, lighter material form shells around it.

is formed, it can react with another proton in the reaction ${}^2D + p- >{}^3 He + \gamma$. At this point the reaction chain splits of into the main paths. In the path, pp1, ${}^4He$ is created through the reaction ${}^3He + {}^3He \rightarrow {}^4He + 2H$ [7]. The second path, pp2, has a few more steps. The ${}^3He$ first fuses with an environmental ${}^4He$ creating ${}^7Be$ and γ-rays as ${}^3He + {}^4He \rightarrow {}^7Be + \gamma$ [7]. Then the ${}^7Be$ β^- decays into ${}^7Li$ and a neutrino. The ${}^7Li$ can then capture a proton to make ${}^8Be$, an unstable isotope that decays into two ${}^4He$ nuclei [7]. The last and longest of the hydrogen fusion chains we will discuss, pp3, also has the ${}^3He + {}^4He \rightarrow {}^7Be + \gamma$ reaction. However, unlike pp2, the created ${}^7Be$ then captures a proton making ${}^8B$ in the reaction ${}^7Be + p \rightarrow {}^8B + \gamma$. The boron then beta decays into ${}^8Be$ which, as stated before, becomes 2 ${}^4He$ nuclei [7].

3.2.1.2 CNO cycle

Younger stars which have formed from the remnants of older stars may have initial isotopic abundances that are not only from BBN but are also enriched by fusion that occurred in their parent. If the enriched material is in the C, N, and O mass region, then those nuclei can be involved in creating ${}^4He$ as well. This group of four reaction chains are known as the CNO cycles [7].

Once the hydrogen fuel in the core is fully depleted, the core is now made of Helium, and the star

leaves the main sequence. Stars with $M_s < 0.23 M\odot$ are believed to directly become white dwarfs ; however, since their lifetime is longer than the age of the universe there is no direct observation [64]. In more massive stars with a Helium core, the star has now entered the Red Giant Branch (RGB). A shell of hydrogen around the core can continue fusing or "burning" which will cause outer layers to expand. As the hydrogen shell keeps burning, the Helium core grows more massive and heats, which accelerates the shell burning. The CNO reaction chain can take a different path at higher temperatures. In this hot CNO (HCNO) path proton and alpha captures can dominate over positron decays leading to an abundance of proton rich nuclei [65].

3.2.2 Helium fusion

Helium fusion occurs under the triple alpha process (3α) which, as the name suggests, is the fusion of three helium nuclei. The fusion must occur this way because, while the probability for only two helium nuclei to collide and fuse is much higher, the reaction product, ^8Be, is highly unstable. In the triple alpha process, all three helium nuclei fuse together in a time shorter than the half life of ^8Be to create ^{12}C:

$$3\ ^4He \rightarrow\ ^{12}C$$

or

$$^4He +\ ^8Be \rightarrow\ ^{12}C$$

This reaction proceeds through a resonance in ^{12}C known as the Hoyle state [66]. ^{12}C is the primary reaction product; however, some of it can react with ^4He creating ^{16}O in the core.

3.2.3 Other Stellar Burning

Stars with mass ≥ 2 solar mass can 3-alpha before degeneracy leading them onto the asymptotic giant branch (AGB). Fusion to higher mass isotopes occurs in similar fusion processes sequentially in Carbon, Neon, Oxygen and Silicon burning phases. The most massive stars create $^{56}Ni/\ ^{56}Fe$ cores at which point fusion no longer provides any star with enough pressure to resist the force of its own gravity [7]. Less massive stars may end at any point before if the core temperature is too low to trigger the next burning phase.

For stars that can fuse an Iron core, the star's mass determines its next form. The lightest of these massive stars undergo core collapse supernovae (CCSN). No longer supported by fusion pressure, the material above the core rapidly accelerates toward the center. Unable to overcome the electron degeneracy pressure of the dense core, the material bounces of and ignites in a large explosion. When stars of even greater mass collapse, the force of the surrounding material overcomes the electron degeneracy pressure supporting the Iron core and it collapses as well. For massive stars in the intermediate range this collapse halts once nucleons become degenerate, forming neutron stars. The most massive stars collapse further still, creating black holes.

3.3 Nucleosynthesis Beyond Iron

The stellar burning phases described thus far can only create elements up to Fe; however, many more than 26 elements exist (e.g gold, copper, lead). This leads to a rather obvious question: Where did the heavy elements come from? The B^2FH paper [4] proposed 3 major processes that can produce isotopes beyond ^{56}Fe are produced: the rapid neutron capture process (r-process), the slow neutron capture process (s-process), and a proton capture process (p-process) which is now known to be a series of photodisintegration reactions and is sometimes called the γ-process.

3.3.1 s-process

In the s-process path, when an isotope captures a neutron, a radioactive child nucleus is likely to β^--decay before another neutron can be captured. The slow neutron capture rate is due to the s-processes sites having a low neutron density $\rho_n \approx 10^{7-11}\ cm^{-3}$. The starting "seed" nuclei of the s-process are grouped in what is known as the Iron Peak nuclei (e.g. ^{56}Fe, ^{56}Ni). Because of the requirement of iron peak seed nuclei, the s-process in called a secondary process; it cannot occur without stellar fusion happening first. Since capture is slow, the s-process path remains close to the stable isotopes. The first confirmed s-process site is in AGB stars; whose spectra show evidence of the production of radioactive Tc [67]. The s-process is considered to be responsible for ≈50% of heavy element isotopes.

3.3.2 r-process

The r-process occurs in explosive events with a neutrons neutron densities $\rho_n \approx 10^{20-22}\ cm^{-3}$. The high capture rate causes the r-process path to move to neutron-rich nuclei far from stability, until it reaches equilibrium with the reverse (γ, n) reaction. Once the environment loses sufficient neutron density to continue the r-process, β-decays bring the population of exotic isotopes to heavier stable elements. Potential sites of the r-process has been an open question since the B^2FH paper. Suggestions include core collapse super novae, neutron star mergers, and even black hole mergers as candidates. On August 8th 2017, the LIGO collaboration detected gravitational wave event GW170817 caused by two neutron stars merging. Spectroscopic data collected from this event showed clear evidence of r-process nuclei forming [68]. While neutron star mergers are a confirmed r-process site, it is unclear how much they contribute to the overall r-process element abundance as well as the contribution of other potential sites [69].

3.3.3 γ-process

There are a series of stable, neutron deficient nuclei that cannot be produced by either the s or r processes. The B^2FH paper identified these 35 nuclei, now known as the p nuclei. In their work, the process of creating the p nuclei was described as a series of proton capture and neutron emission events on s and r process seed nuclei. However, further research determined that the conditions needed for this reaction path were improbable in hydrogen rich areas of most stars [70]. Instead, an alternative process based on photodisintegration reactions on heavy nuclei was suggested. This γ-process is now considered the main mechanism that creates the p nuclei. As a tertiary process, it does not use iron peak nuclei as a starting point, but rather nuclei at the end points of the s and r processes. After either process, the created material will be ejected into the interstellar medium (ISM). Protostars can form out of this heavy element enriched material and create stars with s and r process isotopes mixed throughout its volume. These isotopes are the seeds for the γ-process path. The path is defined by a series of proton, neutron, and $\alpha(^4He)$ emissions triggered by high energy γ-rays during an explosive event. Early on in the process, neutron emission dominates. As the path moves to more neutron deficient isotopes, removing a neutron becomes more difficult. Eventually,

emitting a proton or α becomes a more likely next step on the path as the energy to remove another neutron rises. Through this path, the γ-process creates lighter, stable p nuclei from heavy seeds.

3.4 Other Nucleosynthesis processes

Beyond these original three processes, several more have been discovered, including intermediate neutron capture process (i-process) [71], the rapid proton capture process (rp-process) [72], and the neutrino proton capture process (νp-process) [73]. The focus of this thesis is on proton rich side of the valley of stability. The investigation is on the reaction $^{59}Cu(p,\gamma)^{60}Zn$, a branching point (or fork) along the rp and νp process paths. The reaction rate here determines if the path continues up toward heavier mass isotopes or if instead the proton knocks out an α particle leading to lighter mass isotopes [74]. This competition is important not only for modeling light curves from Type-I X-ray bursts but also in determining the composition of neutron stars.

3.4.1 rp-process

The rp-process is the the major fusion and energy production mechanism of Type-I X-ray Bursts. These events are the most common explosive occurrences in the Milky Way; however, the isotopes produced contribute very little to isotopic abundances [72, 75]. Type-I X-ray bursts occur in binary star systems of a neutron star and main sequence partner. When the partner overfills its Roche lobe, the material outside is no longer gravitationally bound to it and instead accretes onto the neutron star through Lagrange point L1, the center of mass of the binary system. The material (mostly Hydrogen and Helium) accelerates under the intense gravitational pull and forms an accretion disk around the neutron star in the plane of orbit of the binary system. As the material lands on the surface of the neutron star, it heats to temperatures ranging $T_9 = 0.7 - 1.5$ [75] and begins fusion through the HCNO cycle. While this occurs, mass is still being accreted and a degenerate shell of matter quickly forms and temperatures continue to rise. The triple-α process then dominates the reaction, causing a helium flash. While a flash on a main sequence star leads to material being ejected across the ISM, the intense gravity of the neutron holds the material tight, causing a thermonuclear runaway. The runaway breaks out from the HCNO cycle through the αp-process, a process dominated by α capture reactions [74]. From there on the rp-process begins. This process

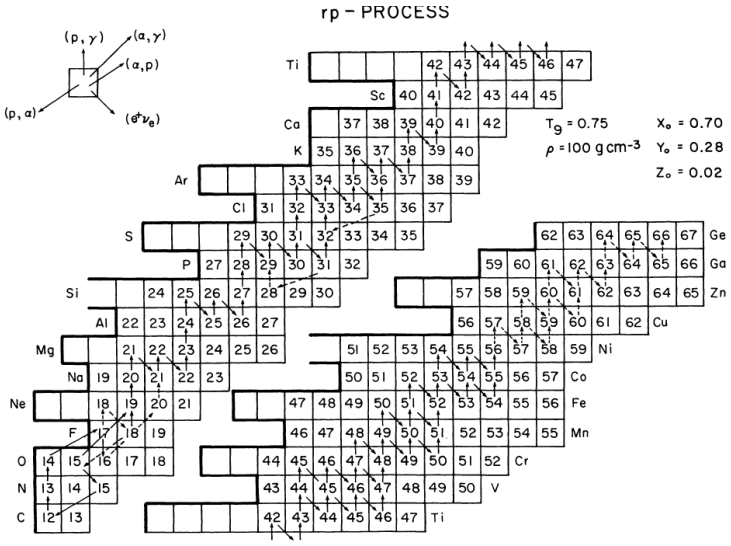

Figure 3.2 Reaction flow of rp process. [76]

is dominated by proton capture and β^+ decays beginning at ^{19}Ne at temperatures favorable for $^{19}Ne(p,\gamma)^{20}Na$[75] leading to a calculated end point in neutron stars near mass A = 107, where the path becomes a loop, cycling through Sn, Te, and Sb [77].

3.4.2 νp-process

In the inner ejecta of a core collapse super novae (CCSN) and neutrino winds of a proto neutron star, an abundance of proton rich matter can form from neutrino captures [78]. As it cools, the environment is mainly composed of N ≈ Z isotopes (e.g ^{56}Ni, ^{4}He) and protons [73]. The protons capture antineutrinos becoming neutrons, which are preferentially captured by the proton rich isotopes in (n,p) reactions [79]. The (n,p) reactions lead to a higher net proton capture rate of the material, and the process moves toward heavier nuclei [80]. The νp-process can also form some of the p nuclei of the γ-process [81].

3.5 NiCu Cycle

Both [79] for the νp-process and [77] for the rp-process report that the competition between the $^{59}Cu(p,\gamma)^{60}Zn$ and $^{59}Cu(p,\alpha)^{56}Ni$ reactions can lead to a NiCu cycle if the (p,α) reaction is dominant. The rp process NiCu cycle is illustrated in Fig. 3.3[74]. The νp-process NiCu cycle takes the path [79]:

$$^{56}Ni(n,p)^{56}Co(p,\gamma)^{57}Ni(n,p)^{57}Co(p,\gamma)^{58}Ni(p,\gamma)^{59}Cu(p,\alpha)^{56}Ni$$

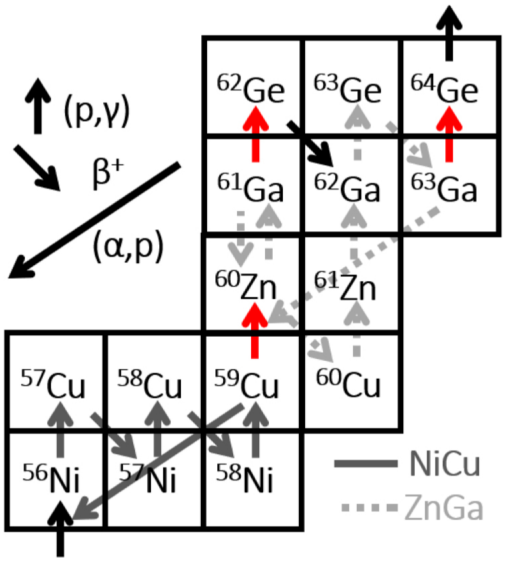

Figure 3.3 Reaction Flow of the rp-process around ^{59}Cu [74]

This would significantly limit the abundance of isotopes above A=56 created in both processes. For Type I X-ray bursts, this has a large impact on the Type I X-ray Burst light curves and the thermal profile of neutron star crusts [81]. For CCSN, the contribution to the p nuclei abundance would be limited to the lighter isotopes and would not flow past ^{59}Cu at temperatures $\approx$ 3 GK [79]. The $^{59}Cu(p,\alpha)^{56}Ni$ has previously been measured at astrophysical energies [81, 82]; however, there are no constraints for the $^{59}Cu(p,\gamma)^{60}Zn$. At rp-process temperatures, the cross section is on the order of 0.1 micro barn, making it challenging to measure directly. The present thesis focuses on an experiment to constrain this reaction indirectly.

CHAPTER 4

EXPERIMENTAL DETAILS

The data for this thesis was obtained during National Superconducting Cyclotron Laboratory (NSCL) experiment e17009, performed in 2019. The facility generated a primary beam of $^{78}Kr^{36+}$ by accelerating particles from a spallation source with a pair of coupled cyclotrons [83]. The primary beam then impinged on a ^{9}Be target to create a secondary beam. This secondary beam was filtered through the A1900 fragment separator to remove contaminants resulting in a beam of ions with $A \approx 55$. Since the desired beam was ^{60}Ga, a second filtering step was applied using the Radio Frequency Fragment Separator (RFFS) to further improve beam purity [83, 84]. This chapter will provide a description of the NSCL beam line and the detectors used in the experiment.

4.1 Beam Production

4.1.1 Coupled Cyclotrons and Primary Beam

The NSCL had two electron cyclotron resonance (ECR) ion sources, the ECR ion source (ECRIS) [85] and the Advanced Room-TEMperature Ion Source (ARTEMIS) ECR [86]. Source ions were injected into the center of the cyclotron. Cyclotrons have three basic parts: two metal D's (named for their shape), an azimuthal electric field, and a gap between the Ds. When ions are injected into the gap, they are accelerated by the field into a D. From Gauss' Law, we know that there is no electric field inside a conductor, therefore the ions drift at a constant velocity with respect to center inside the D. Once they exit, they are once again accelerated and their radius increases to conserve momentum. The strength of the field filters source ions by momentum and charge (Bρ); ions with unwanted ratio will either crash in the wall of the cyclotron or exit at a rate much lower than the desired ions with the desired ratio.

The NSCL had two cyclotrons (K1200 and K500) coupled together to provide higher intensities for heavy common and exotic ion beams [84]. This produced the primary beam of the present work, $^{78}Kr^{36+}$, at 150 MeV/u with an intensity of 5pnA. The primary beam then impinged on a 705 mg/cm^2 ^{9}Be target to produce a secondary "cocktail" beam of various ions $A \approx 55$.

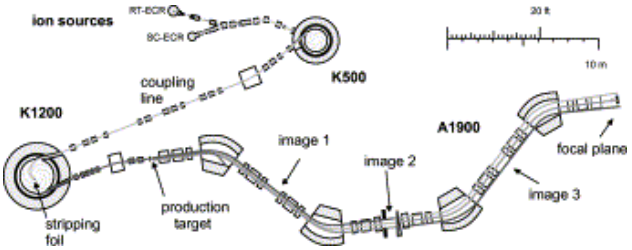

Figure 4.1 NSCL beam line. From A1900 paper

4.1.2 Fragment Separators

After the production target there were still many contaminating ions that would make data collection extraordinarily difficult. Therefore, the beam needed to be purified as much as possible. To accomplish this, fragment separators were used. The A1900 fragment separator was standard in almost every NSCL experiment. In addition experiment e17009 also included the RFFS had capabilities that specifically benefit experiments using neutron deficient beams.

4.1.2.1 A1900

The A1900 fragment separator was installed in the NSCL beam line in 2000 replacing the A1200 fragment separator. The A1900 was made of 24 quadrupole magnets and 4 dipole magnets set at 45° in the azimuthal direction [84]. The strength of the magnetic field was set to allow only ions in a range of momentum to pass through. The A1900 has a large momentum acceptance, so the filtered beam was a cocktail of ions around mass 55 [83].

4.1.2.2 Radio Frequency Fragment Separator [87]

After filtering through the A1900, the cocktail beam comprised of isotopes whose $B\rho$ overlapped with that of our isotope of interest ^{60}Ga. For neutron deficient isotopes the contaminant fraction increases exponentially as the nucleus of interest approaches the drip line. ^{60}Ga was effectively obscured, necessitating a second filtering step. Typically, a wedge was used for energy loss filtering; however, all isotopes in the beam for this experiment would have similar energy losses in matter, so the wedge was ineffective at purifying the beam. The wedge caused a large velocity dispersion in the beam components. Therefore, a velocity filtering method was able to further purify the beam. Other velocity filters (e.g. Wein filter) have been used successfully ; however, they are effective with beam energies $E_{beam} \approx 50 MeV/u$, a third of the beam energy used in this experiment. The Radio

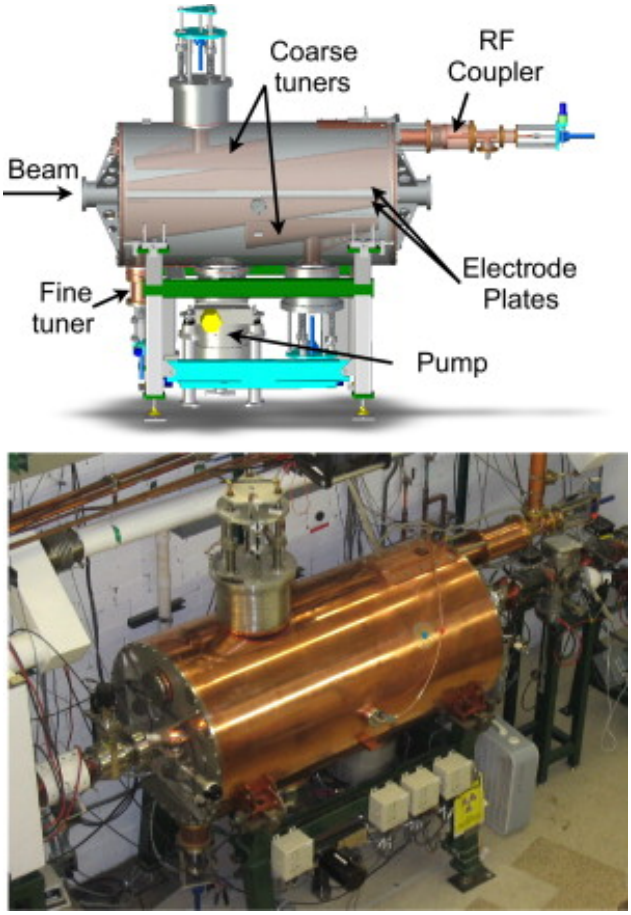

Figure 4.2 Top: Radio Frequency Fragment Separator diagram.Bottom: Photo of the RFFS used in experiment e17009 [87]

Frequency Fragment Separator was able to filter at beam energies in the range that the coupled cyclotrons produced. The RFFS selected isotopes based on their phases which is directly related to their velocity [87]. As beam particles leave the cyclotron, they are all initially in phase with the accelerating RF; but, as progress down the beam line the phase distribution of the isotopes grows broad due to their different velocities. The effect was exacerbated by the wedge. The RFFS applies a transverse radio frequency (RF) field synchronized with the cyclotron RF to the beam. The applied RF field deflects beam particles at an angle based on their phase, filtering out contaminants. Despite this extra filtering, the beam was not pure; however, the isotope of interest was now clearly distinguishable from the remaining contaminants from time of flight (ToF) and energy.

Figure 4.3 PIN detector used in experiment e17009. [88]

4.2 Detectors

As the cocktail beam progresses to the end station, it passes through a number of Si PIN detectors, which provided energy loss and time information. The end station itself comprised of a Double Sided Silicon Strip Detector (DSSD) as an implantation surface and the Summing NaI(Tl) (SuN) Spectrometer measured γ-rays from the de-excitation of the child nucleus.

4.2.1 PINs

PIN detectors are photodiodes with an undoped intrinsic semiconducting region between p and n type semiconducting regions, that convert ionizing radiation into an electrical signal. In this experiment, two silicon PINs were used to detect the energy loss of beam particles before entering the volume of the Summing NaI(Tl) Spectrometer. The PINs had thicknesses of 488μm and 503μm. The time data from one PIN was used with time data from the focal plane of the A1900 to determine the time of flight of the beam particles. The time of flight was used in conjunction with the energy loss to identify the various ions in the cocktail beam.

4.2.1.1 Double Sided Silicon Detector

After passing through the PINs, the beam stops on a Double Sided Silicon Detector (DSSD). The DSSD used was 1 mm thick, comprising of two layers of 16 silicon strips; each strip being 1.2 mm wide. The layers of silicon strips are positioned orthogonally creating a pixel structure that allows for 2D position tracking. Signals from the DSSD were read into dual gain preamplifiers,

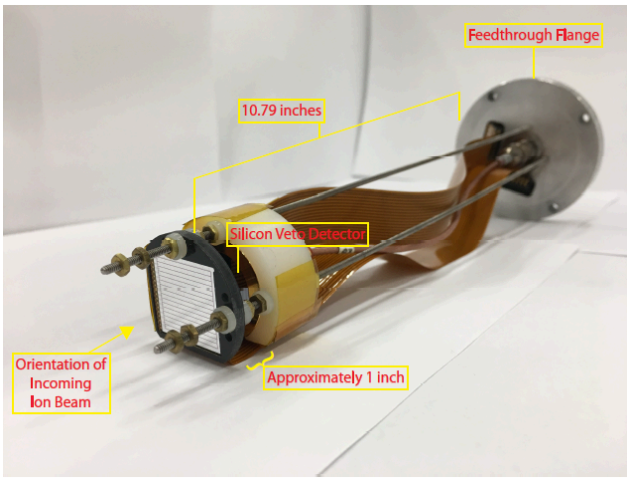

Figure 4.4 Double Sided Silicon Strip Detector set on flange. The Veto detector behind the DSSD rejects data from anything it records. Image from [88]

allowing for concurrent detection of implants and decay products. Beam particles implanted in the detection material depositing their energy into a DSSD pixel. The strips that make up this pixel read out the implantation energy into low gain data channels. The beam particle then decays on the DSSD emitting a beta particle and γ-rays from the child nucleus. The β^+ particle and γ-rays enter the NaI crystals in SuN. The energy of the child nucleus was measured in the high gain channels of the DSSD. The high and low gain DSSD signals are then processed through dual gain preamplifiers, allowing for concurrent measurement of implant particles and decay product. Behind the DSSD was a silicon surface barrier detector which functioned as a veto detector. The veto detector recorded any ions that passed through the DSSD so their contribution to the data could be removed in the analysis.

4.2.2 Summing NaI(Tl) Spectrometer

The Summing NaI(Tl) (SuN) Spectrometer is a $16in \times 16in$ cylindrical detector; housing 8 large semi circular NaI(Tl) crystals. SuN has nearly 4π angular coverage (98% at the center), with a 1.8 in diameter bore hole along the beam axis for the beam line to pass through [89]. Its large NaI(Tl) crystals and large angular coverage make SuN ideal for Total Absorption Spectroscopy (TAS) measurements.

For γ-ray spectroscopy experiments, there are several different options for detection material,

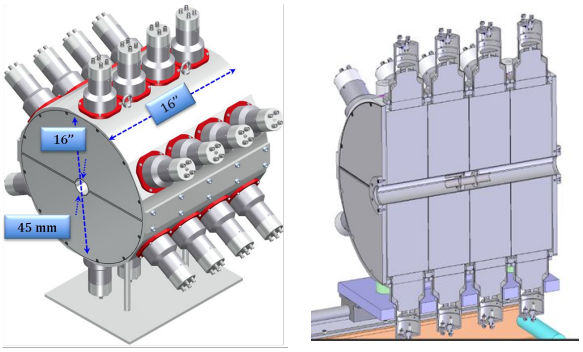

Figure 4.5 The

depending on the specific needs of each experiment SuN's NaI crystals have a resolution of ≈ 5.8% at 1.33 MeV and a full energy summing efficiency of 85(2)% [89]. They can also operate at room temperature, so they can be easily transported to various beam lines or laboratories and do not require hours of cooling time before functional.

The NaI crystals in SuN are wrapped in a 0.5 mm layer of aluminum that are covered in 0.25 mm of reflecting material to optically isolate them into 8 independent segments [89]. The reflecting material serves to decrease the rate of γ-ray escape or incomplete energy deposition. The isolated top and bottom four segments are then wrapped together in another aluminum layer, creating the two halves of SuN. Three photo multiplier tubes (PMTs) are placed on each segment at a spacing of 60° with respect to the center of the bore hole. Each PMT has a separate high voltage (HV) supply for gain-matching 5.1.1. The signals from each PMT in a single segment were summed in offline analysis to remove position dependence.

4.3 Event Correlation

Signals in the various detectors needed to be correlated into a single event in the data. A DSSD implantation event was defined to have a signal in both PIN detectors and a low gain signal from each layer of the DSSD and a decay event. In contrast, a DSSD decay event was defined as having no signal from either PIN and a high gain signal from each DSSD layer. Once a decay event was recorded it was associated with the nearest implant event within a 400 ms time window. This time window was large compared to the previously measured ^{60}Ga half-life of 70 ± 15ms [90] and minimized uncorrelated data [83]. It was possible that the decay event was not actually associated

with the implant event to which it was correlated but instead to some other ion implant. To account for this, so called "random" correlations were created as an alternative to a background spectra. To create the random correlations decay events are matched to implant events that were recorded at a future time within the 400 ms time window.

CHAPTER 5

TOTAL ABSORPTION SPECTROSCOPY: ANALYSIS & RESULTS

The first goal of this work was to determine the structural properties I_β and B(GT) of the beta decay of ^{60}Ga into ^{60}Zn. These features were ascertained with Total Absorption Spectroscopy (TAS) analysis 5.2. This required simulating $gamma$-ray cascades and modeling SuN's response to these events. The simulation was performed with RAINIER(Sec. **??**sec: RAINIER [25] and the modeling with GEANT4 (Sec. 5.2.2) [91].

5.1 Analysis

5.1.1 Gain Matching and Energy Calibration

Analysis began with standard gain-matching and energy calibration procedures that have been described in detail in Ref. [88, 92] and are summarized here. γ energy in a SuN crystal is measured by its 3 PMTs. While the PMTs are gain matched during the experimental set-up by adjusting high voltage values, slight discrepancies can still exist. These discrepancies can artificially widen peaks in the data. To correct this, γ-ray data from background or source runs from the PMTs on each crystal are aligned by multiplying a scalar to each. In practice, a characteristic peak was identified in the spectra and a scalar was applied to two of the PMTs, aligning the group to the values of one PMT. Once gain matched, the data was calibrated onto the energy axis by using known sources. The sources used in this work were ^{241}Am, ^{137}Cs, ^{60}Co, and ^{207}Bi. A linear fit was performed on these values to create mapping to shift all measured energy values into the correct units.

5.1.2 Particle Identification

The cocktail beam that implanted on the DSSD was comprised of several isotopes near A=59. The particle identification using the time-of-flight on the x axis and the energy loss of the beam particle through one of the PIN detectors on the y-axis as in Fig.**??**. The individual clusters correspond to different isotopes in the beam. In Fig.**??**, the clusters lesss than 9 000 on the time of flight axis are long lived stable isotopes, the cluster outlined in black is ^{60}Ga. . By using the graphical cut feature in ROOT to form gates around each region, a gate was formed that isolates the data of one isotope from the others in the cocktail beam. Isotopes are identified by comparing

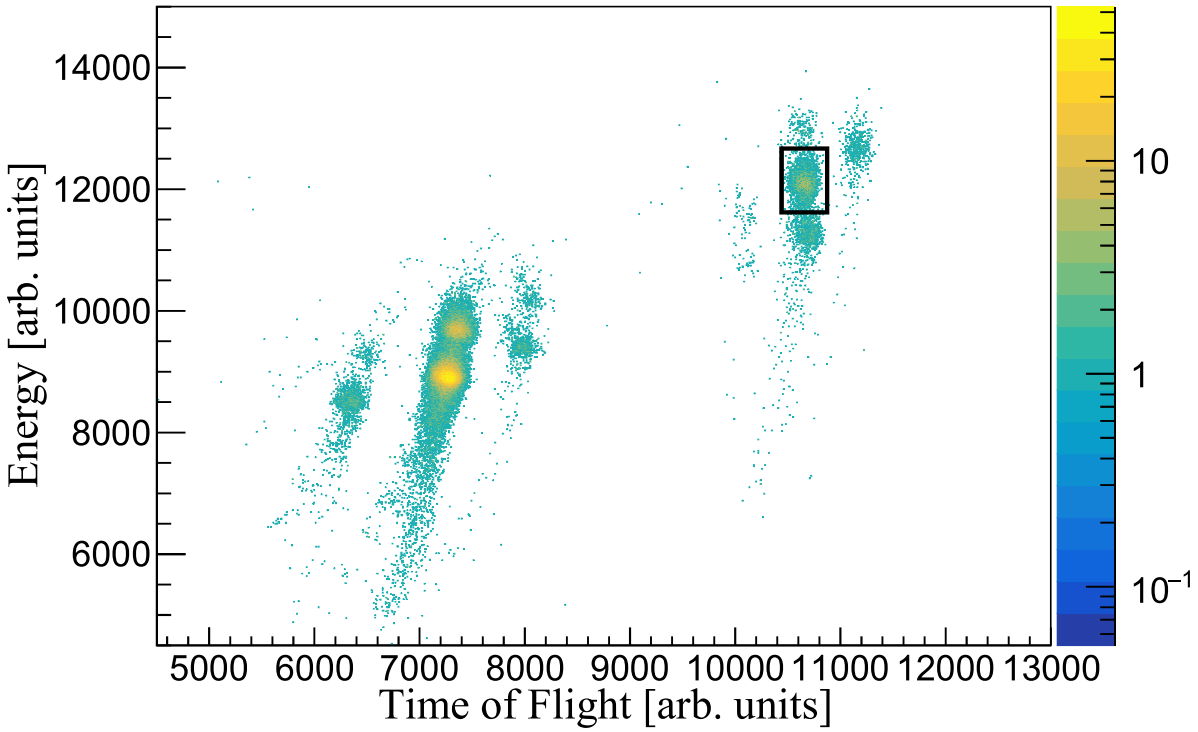

Figure 5.1 Particle Identification plot of the cocktail beam produced in e17009. The time of flight was determined from signals in the A1900 focal plane and PIN detectors. The vertical axis is the energy deposited in the PIN by beam particles. The isotope of interest ^{60}Zn is highlighted in the black box. Isotopes in the bottom left are long lived contaminants.

data with known half-lives and / or characteristic γ-ray measurements listed on NNDC.

5.1.2.1 Half-Life

Plotting the time between implantation of the ion and the correlated decay event with an isotope gate shows the decay rate of the isotope. After background subtraction, fitting the resulting curve with a exponential leads to the half life of the isotope. Comparing this value to reported half lives in NNDC for the mass region verifies the PID. The fit was done in ROOT using the expo and pol0 terms, which corresponds to an exponential fit to match the shape of the decay with a linear polynomial that accounts for the shape of the background. This fit was applied over several bin sizes and regions across the 400 s correlation window. From averaging these fits and accounting for their respective uncertainties, a half-file of 57.7 ± 9.8 ms was extracted from the data. The accepted half-life of ^{60}Ga is 69.4 ms [93] and previous measurements determined it was 70± 15

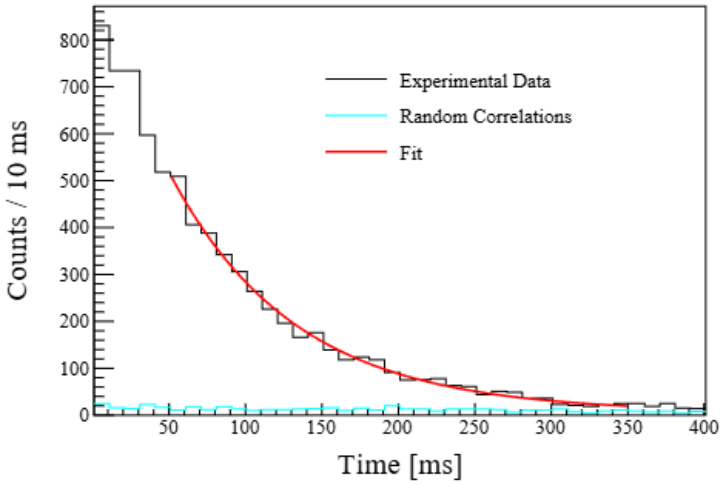

Figure 5.2 Correlated time plot of ^{60}Zn isotopes. The fit was performed using an exponential fit for the decay shape plus a linear term to account for the shape of the background. The half-life was calculated to be 57.7 ± 9.8 ms

ms [90], 69.4 ± 2 ms [94] and 76 ± 3 ms [95].

5.2 Total Absorption Spectroscopy

The TAS technique is a helpful tool that solves the so called Pandemonium Effect [96]. When studying β decay events with high Q values such as $^{60}Ga(\beta^{+})^{60}Zn$, an excited child nucleus is likely to emit many γ-rays at energies outside of the range where High Purity Germanium detectors are effective [96]. Therefore, calculating the initial excitation energy of the child nucleus becomes difficult. The incomplete summing that results is the definition of the Pandemonium Effect, and leads to inaccurate conclusions on aspects of the structure such as the β feeding intensity (I_β). The geometry of SuN, along with its large NaI crystals, allows it to absorb the totality of emitted γ-ray within its volume. Therefore, a more accurate I_β can be determined by collecting data with SuN than with detectors of other materials or less angular coverage.

The isotope gate is also used on γ spectroscopy data from SuN to visualize the isotopes excitation energy, individual γ-ray energy, and multiplicity. Performing a χ^2 fit of GEANT4 simulations to the gated data determines the I_β feeding as described in Sec. 5.2.3.

5.2.1 RAINIER

To model ^{60}Zn continuum levels in GEANT4, it is necessary to simulate how the nucleus de-excites from these high energies. The **Randomizer of Assorted Initial Nuclear Intensities and Emissions of Radiation (RAINIER)** is a Monte Carlo code that simulates cascades of emitted γ-rays from excited states of a given nucleus [97]. To account for the statistical nature of this process, RAINIER includes parameters that determine how many times a γ-ray cascade should be simulated and how many times the nucleus should be regenerated, varying structural properties where they are unknown.

The simulation process has five steps:

1. Build the low-energy (discrete) region from available data,
2. Use NLD models to construct an artificial level scheme in the continuum region,
3. Populate a user-defined excitation energy in the simulated nucleus,
4. Use γSF models to simulate de-excitation to the ground state,
5. Calculate and record the emitted γ-rays.

The major advantage of RAINIER in this analysis is that it calculates simulated deexcitations of cascade paths for a large sample of continuum excitation energies of the nucleus of interest. This information is crucial when simulating the SuN detector response when attempting to reproduce experimental data.

5.2.1.1 Constructing the Discrete Region

To construct the low-energy region of the level scheme, RAINIER requires information on the energy, J^{π}, and decay branches of the discrete states of the nucleus. The **Reference Input Parameter Library (RIPL-3)** provides this information and much more for thousands of nuclei across the nuclear chart [98]. For RAINIER, RIPL-3 can generate a file listing all known and theorized energy levels of an isotope.

For full compatibility, the file must be slightly edited. The half-life ($T_{1/2}$) column is often blank, but RAINIER requires a value. In this work, $T_{1/2} = 1 \times 10^{-15}$ s was used for all levels—long with respect to emission processes but too short to be metastable.

5.2.1.2 Constructing the Continuum Region

While the discrete region is built from the RIPL-3 file, the continuum must be generated by modeling. RAINIER allows users to select between the **Constant Temperature Model (CTM)** [97]:

$$\rho_{\mathrm{CTM}}(E) = \frac{e^{(E-E_0)/T_0}}{T_0}$$

where E_0 is the backshift parameter and T_0 is the temperature; and the **Back-Shifted Fermi Gas (BSFG)** model [97]:

$$\rho_{\mathrm{BSFG}}(E) = \frac{e^{2\sqrt{aU}}}{12\sqrt{2}\sigma}\, a^{-1/4} U^{-5/4}$$

where $U = E - E_1$ is the effective excitation energy, E_1 is the backshift, σ is the spin cutoff, and a is a level-density parameter related to single-particle level spacings.

Both a and σ can be user-defined, and σ has five model options. In addition to CTM and BSFG, users may import a custom level-density table or define their own function with parameters E_0 and T_0.

The underlying distribution of J values is determined by a Fermi-gas model, and the parity is determined either by parity equipartition ($\pi = 1/2$) or by an energy-dependent function:

$$\pi(E, J, \Pi) = \frac{1}{2}\left(1 \pm \frac{1}{1 + e^{C(E-D)}}\right)$$

where C and D are free parameters, and the $\pm$ sign depends on the sign of Π and if the mass number is even or odd. With $\rho(E)$, Π, and J distributions, RAINIER determines the number of levels near an energy E for each J^π. The level density models describe the nuclear structure above the discrete region. Spin cutoff models determine the width of the spin distribution.

5.2.1.3 Populating Levels

RAINIER offers several options in its input file to populate the compound nucleus. To accurately simulate the experiment, the method should match the formation process. For β-decay, the

`bEXSelect` option is most appropriate, allowing multiple initial excitation energies, J^{π} values, and branching ratios.

5.2.1.4 γSF Models

γSF models determine how continuum states de-excite. RAINIER assumes that the decay of a level is independent of its population mechanism. The code includes several E1 γSF models such as the Brink–Axel and Generalized Lorentzian forms; custom models can also be added.

5.2.2 GEANT4

GEANT4 is a simulation toolkit for modeling how materials respond to interactions with radiation or particles. Materials can be defined with specific geometries to model real detectors [91]. Using GEANT4, a model of SuN can be constructed to simulate how γ-rays interact with the NaI(Tl) crystals and surrounding materials.

5.2.2.1 Setting Up the Environment

GEANT4 consists of several header and source files that can be modified to represent the experimental setup. Header files declare classes and functions, while source files define their implementation.

5.2.2.2 Creating Input Files

An input file is created for each excitation energy in the child nucleus, including all discrete states and sampled continuum energies simulated by RAINIER. These files list γ-ray cascades and branching ratios to simulate realistic de-excitations in the detector.

The first line specifies: (1) the total number of cascades, (2) the number of cascades to be read by GEANT4, and (3) the number of γ transitions per cascade.

For discrete states, each line begins with the cascade branching ratio followed by γ-ray energies in emission order. Shorter cascades are zero-padded to match the expected length.

Continuum-level input files are generated by reading RAINIER output and reformatting into GEANT4 style. The first number in each line represents the reciprocal of the total number of cascades simulated, rather than a branching ratio, because each RAINIER cascade (including duplicates) is included.

5.2.2.3 Output

GEANT4 outputs ROOT files containing histograms of:

- Total energy absorbed (compound nucleus excitation energy),
- Sum of segment energies (individual γ energies),
- Multiplicity (number of segment that recorded per event).

Separate output files are generated for each population energy, including the ground state. These served as inputs to the χ^2 minimization process.

5.2.3 χ^2 Minimization

To begin the χ^2 minimization, Experimental and simulated data are converted to histograms. Once histograms are prepared they are fit to the data. TAS, SoS, and multiplicity histograms can be fit independently or in combination. The normalized weights correspond to the I_β feeding strength of each state.

This process is analogous to assembling a puzzle: the experimental data represent the final image, the simulated states are the pieces, and the fitted weights indicate how many of each piece are needed.

Poor fits could indicate missing or inaccurate simulations in certain regions; improving these requires modifying the input set and repeating the χ^2 fit.

5.2.3.1 Experimental γ Spectra

The gated experimental γ spectra were also used to identify isotopes. The gated total absorption spectra have large peaks at energies that correspond to the energy levels of the isotope. γ-ray spectra have some important features arising from the physical conditions occurring within the detector. The energy spectra from β particles recorded by SuN is found across the plot. This feature is created from e^- or e^+ with energies up to the reaction Q value entering SuN. The annihilation peak is located in the TAS spectra at 1.022 MeV and in the Sum of Segments spectra at .511 MeV. These peaks signify the energy detected from an e^+ annihilating with an e^- within the detector volume and releasing their full mass energy. The Compton region, created by the partial energy

deposition of γ-rays scattering within the scintillator material. The end of this region, known as the Compton Edge, represents the full back scatter of photons. The last important feature are the characteristic γ-rays emitted from nuclear de excitations. At low energies, these peaks are easily separable; however, as the number of levels increases with energy, the detection system can no longer resolve individual states.

Comparing the peak energies with known data identifies which isotope was gated. For proton-rich isotopes like ^{60}Zn, it is important to account for the annihilation energy in the peak value before comparison. The key feature of the ^{60}Zn nucleus is its characteristic γ peak near 5.8 MeV in the TAS spectra Fig.**??**a. This peak is a combination of de excitation from the 4.8 MeV IAS and annihilation energy.

Previously, data on this β-decay was limited to the half-life and I_β feeding to levels up to the IAS [90, 94, 95].

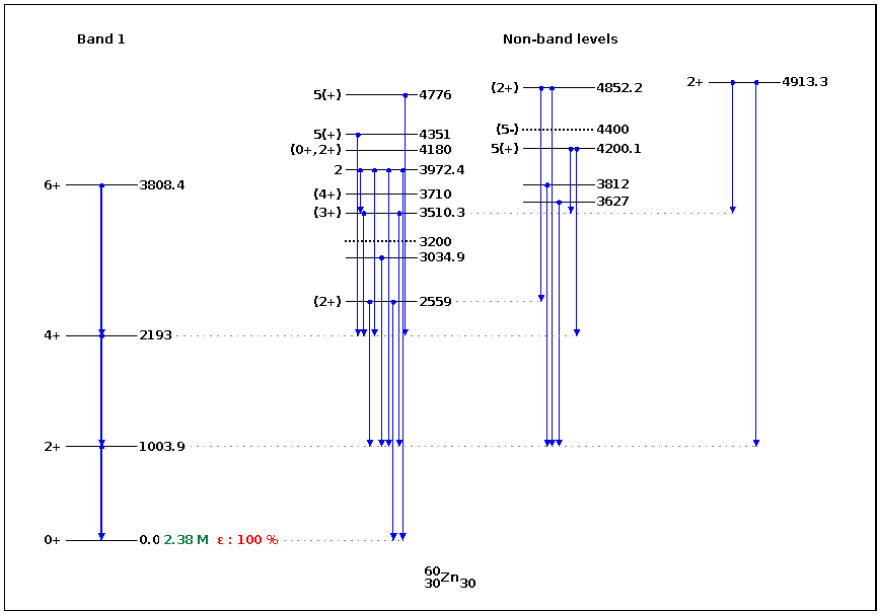

Figure 5.3 Discrete level scheme of ^{60}Zn used in RAINIER simulations. Generated in NNDC [93].

5.3 Calculation and Recording

Determining the contributions of the various populated states to the experimental spectra required simulating each level independently. Each energy level was simulated first in RAINIER. The RAINIER input had 20 realizations of 100 000 events. In this analysis, the excitation was held

constant for each run, sampled from the continuum region. Three J values ($1^+, 2^+, 3^+$) were chosen to represent allowed β transitions from the parent ground state(2^+), each with equal branching ratio ($1/3$). The Generalized Lorentzian model described E1 transitions and an M1 model accounting for an upbend was used for M1 transitions. The CTM model was used for NLD with $T_0 = 1.371$ MeV and $E_0 = 0.174$ MeV. The rigid-sphere model was adopted for ^{60}Zn. In cases where J^π is uncertain or unknown, several copies of the RIPL-3 file were made, each with different assignments for these states and the results were included in the uncertainty estimate. RIPL-3 indicates that the level scheme of ^{60}Zn is complete up to its 3.972 MeV state; however, this nucleus also has two states at 4.852 MeV and 4.913 MeV with the same J^π as the ground state of the parent nucleus(Fig.5.3). The 4.852 MeV state was considered isobaric analogue states (IAS) and was expected to be preferentially populated by β-decay. Due to this preference, we assume populating these states is non-statistical; therefore, the level scheme was set to be complete up to (and including) the 4.913 MeV state. The simulation output was organized first by RIPL3 file version, then by energy level populated. The crucial output is the gamma ray cascade. This information was used by GEANT4 to simulate how these γ-rays interact with the SuN detection system.

5.4 I_β and B(GT) Results

The results of the TAS analysis on ^{60}Zn are presented below. GEANT4 simulations of ^{60}Ga β-decay to ^{60}Zn were performed for 39 excitation energies. To account for the non-statistical behavior of the IAS near 4.85 MeV, all levels with less energy were treated as discreet states. The energy region above this value was considered as the continuum and simulations were based on energies sampled in this space up to the decay Q value of 13.6 MeV. Simulations for energies above ≈9.8 MeV were removed due to the poor replication of the data in high energies resulting in a total of 33 simulations used in the final fit. Continuum energy simulations were based on RAINIER de-excitation simulations of the ^{60}Zn nucleus. As some $J\pi$ were unknown or uncertain for a subset of discreet states, 10 trials were done. Each trial used slightly altered RIPL-3 files, varying the uncertain $J\pi$ by $J \pm 1$ and changing the sign of the parity. Each trial had its own RAINIER and GEANT4 simulation and was included in the uncertainty calculation in Fig.**??**. Fig.**??** shows just

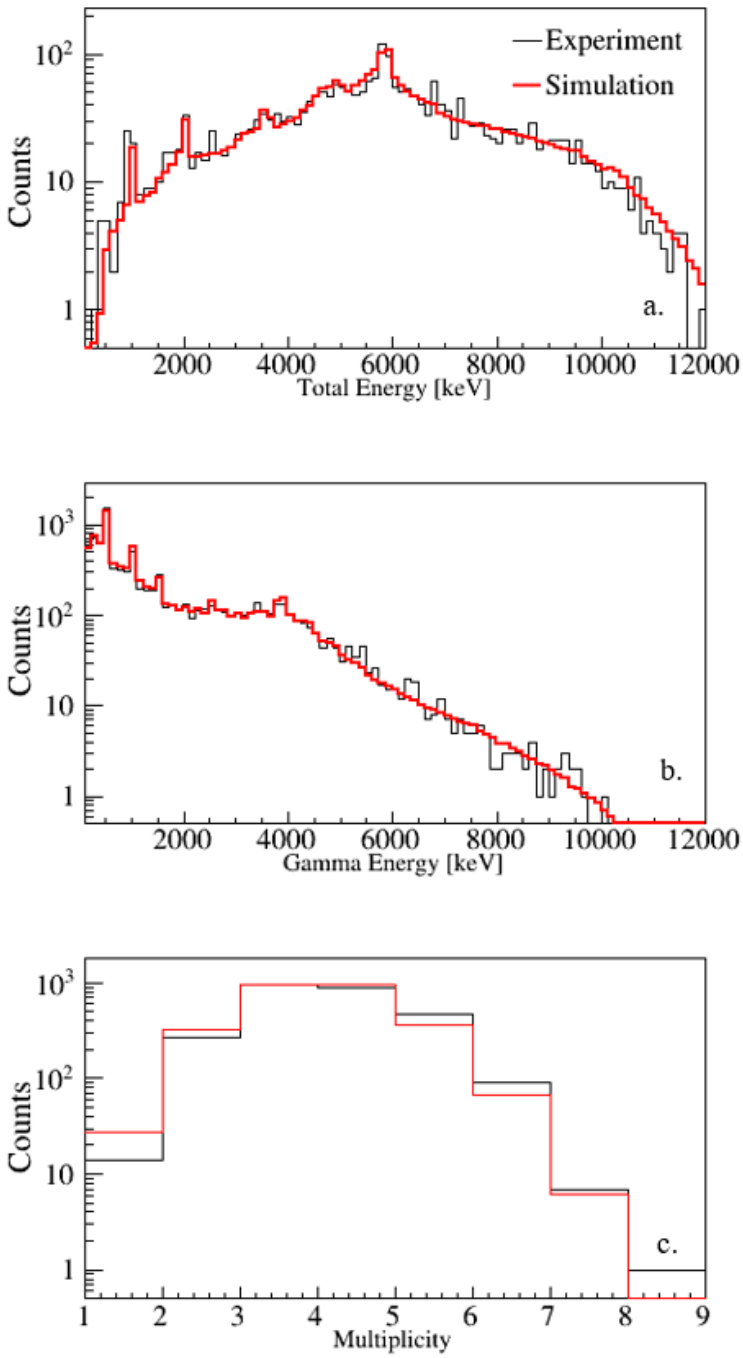

Figure 5.4 Experimental data with χ^2 fits of one set of GEANT4 simulations. The top plot is the total absorption spectra. The peak near 6 MeV corresponds to the IAS with a boost from the annihilation energy. The middle plot is the Sum of Segments showing individual γ-ray energies. The bottom plot is the multiplicity, displaying the number of γ transitions to reach the ground state.

one trial to illustrate fit quality. The data and uncertainty band are an average over the 10 different simulation trials. The uncertainty also includes contributions from statistical uncertainty, detector

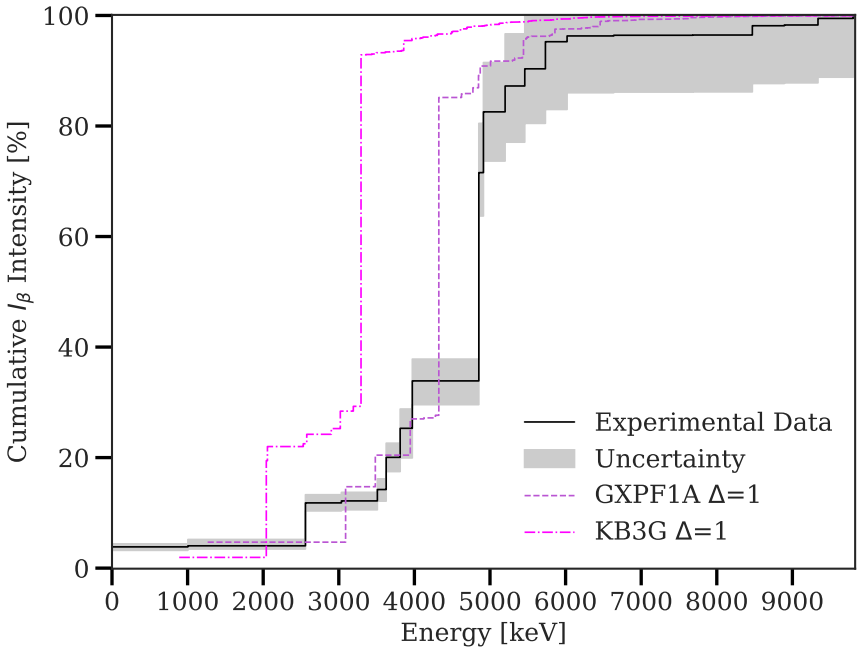

Figure 5.5 Plot of the cumulative I_β transition strength. The data in black and uncertainty in grey, are averages over 10 separate trials of varying $j\pi$ for unknown or uncertain discreet levels. The pink and purple dashed lines are predictions from Shell Model calculations. See Sec.5.4 for details.

efficiency, fit uncertainty,and the distance from average to maximum and minimum at each energy bin. The data (Fig. 5.5) shows a large increase in transition rate at the IAS energy, confirming the Fermi nature of the transition. 12.8% of the feeding occurs above the proton separation energy of 5.1 MeV [83]. This shows that the γ decay channels at high energies still competes with the proton decay channel for $J\pi$ populated through β-decay.

The experimental I_β was compared to Shell Model calculations by Alex Brown with the NuShellX code. The KB3G [99] GXPF1A [100] hamiltonian calculations in Fig.**??** were used on the fp model space and the Δ refers to the number of nucleons excited out of the $0f_{7/2}$ shell. The major difference between the models and experiment is the location of the Fermi transition. The KB3G hamiltonian sets it around 3.3 MeV and GXPF1A predicts the transition close to 4.5 MeV. Outside of this, the GXPF1A calculation agrees quite well with the measurement, especially at low energies, and both hamiltonians reproduce the shape of the data.

The data and models presented in Fig.**??** were converted to B(GT) and compared to QRPA

calculations with various parameterizations. In the shell model calculations, the value of B(F)was set to 2 at their respective predicted IAS energies. As fermi transitions are the dominant contribution to the transition strength for an IAS, the B(GT) contribution at these energies was treated as negligible for both experiment and models. The QRPA calculations used two parameterizations: D3C* [101] for meson nucleon interaction in the ph channel, and NL3 [102] using meson exchange in the ph channel. The NL3 calculation also included a quasiparticle vibrational coupling (QVC) term that has been shown to improve B(GT) and half-life predictions [103, 104]. Once again the GXPF1A calculation has the best agreement with data. The QRPA calculations suffer from a lack of bins, therefore a majority of the contributionwas in a single peak and usually shifted to lower energies. The half life predictions for GXPF1A and D3C* agree will with measurement with t_{GXPF1A} = 64ms and t_{D3C*} = 58.3 ms laying within the experimental uncertainty [83].

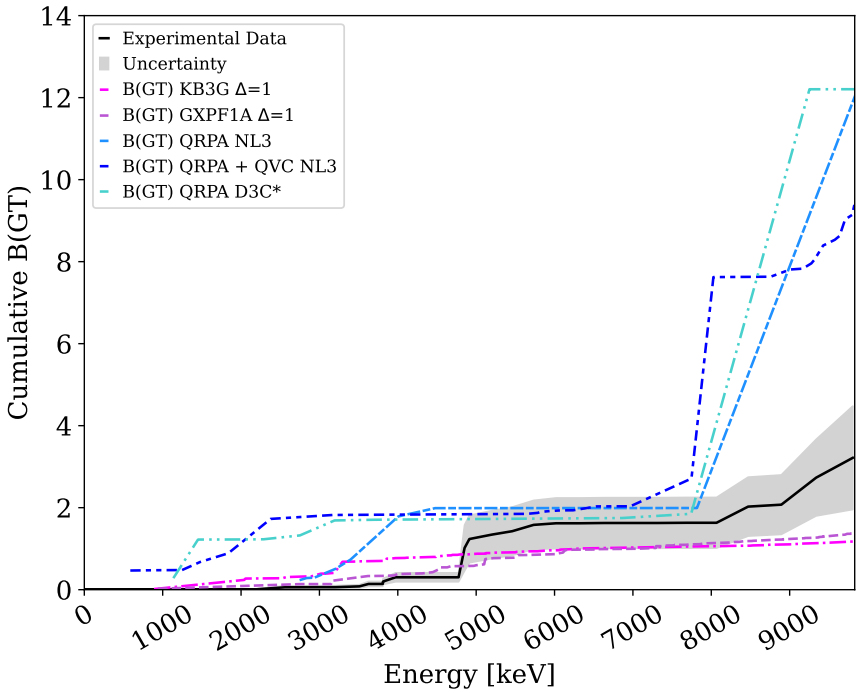

Figure 5.6 Expermental B(GT) compared with various QRPA and Shell model calculations. There is good agreement between the data and all model from 4.8 - 7.8 MeV. The Shell Model calculation lie within the error more, with GXPF1A hamiltonian performing the best.

CHAPTER 6

CONSTRAINT ON THE $^{59}Cu(p,\gamma)^{60}Zn$ REACTION: ANALYSIS & RESULTS

The second objective of this thesis was to constrain the $^{59}Cu(p,\gamma)^{60}Zn$ reaction cross section. The process begins with the extraction of the NLD and γSF through the Oslo Method (Sec. 6.1). Total absorption and sum of segment spectra were input into a modified Oslo method 6.1 for β^+ decays by unfolding the excitation energy axis. Models supplied by the TALYS reaction code [6] were fit to the NLD and γSF. The fitting was performed with a Bayesian inference method summarized in Sec. 6.2. The parameter distributions from the Bayesian posterior were input into TALYS in order to calculate the cross section and reaction rate credible intervals.

6.1 Oslo Method

The extraction of nuclear level densities (NLD) and γ-ray strength functions (γSF) using the Oslo Method involves a series of steps that begin with raw coincidence data from nuclear decay events. The data are initially organized into a two-dimensional matrix of excitation energy E_x (TAS spectra) versus γ-ray energy E_γ(Segment Spectra), commonly referred to as an *Oslo matrix*.

The Oslo Method relies on this matrix as a starting point, but several steps must be performed before NLD and γSF can be extracted. These include detector response unfolding, extraction of the primary γ-ray spectra, and iterative fitting procedures to model the data using known nuclear physics constraints. In β^+ decay experiments, additional complications arise due to the presence of annihilation radiation, requiring modifications to the standard method.

This section outlines the methodology used to convert raw detector data into the quantities of interest. First, we describe the construction of the E_x–E_γ matrix (Sec. 6.1.1), followed by a detailed explanation of the unfolding procedure (Sec. 6.1.2), including corrections for β^+ decay artifacts which are being introduced for the first time here. The extraction of primary γ-ray spectra is discussed in Sec. 6.1.3. These steps form the necessary foundation for the extraction of the functional forms of NLD and γSF presented in Sec. 6.1.4. In the subsequent sections, methods for determining the exact solution of NLD and γSF are discussed.

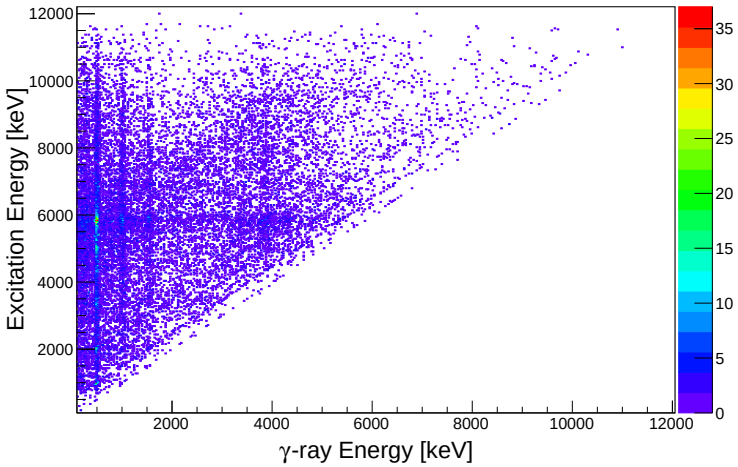

Figure 6.1 Raw Oslo Matrix of ^{60}Zn data. The horizontal axis shows individual γ-ray energy per 30 keV. The vertical axis displays the initial excitation (entry state) energy per 30 keV.

6.1.1 Creating the Ex Eγ matrix

The TAS and Sum of Segments can be plotted against each other in a two-dimensional histogram commonly referred to as an *Oslo Matrix*, with excitation energy on the vertical axis and γ-ray energy on the horizontal. As no γ-ray in a cascade can have more energy than the total excitation energy of the nucleus, the matrix naturally forms an upper triangular shape.

This matrix reveals not only the most probable γ-rays for a given excitation energy, seen as bright bands along horizontal slices indicating strongly populated nuclear levels, but also highlights strong de-excitation from entry states in to discrete levels which appear as diagonal bands parallel to the matrix's hypotenuse. While these features are of general interest, in this work, the Oslo matrix primarily serves as the starting point for the application of the Oslo Method.

6.1.2 Unfolding

The first step in processing the Oslo matrix is the *unfolding procedure*, which corrects for the effects of the detector response. This step assumes that the response of the detector used in the experiment is well understood and accurately modeled. The detector response is represented by a function

$$R(e', e, m, q) \equiv R(E'_x; E_x, M_\gamma, Q_\beta),$$

where e' (or E_x') is the measured excitation energy, e (or E_x) is the true excitation energy, m and M_γ represent the average multiplicity of the excitation bin, and q and Q_β are the Q-value of the β decay[105].

These response functions are generated using GEANT4 simulations of the detection system, performed at various combinations of excitation energies, multiplicities, and Q_β values [91]. Q-values were chosen at 1 MeV steps with multiplicities ranging from 1-5 across randomly selected energies. This provides a comprehensive representation of the detector's behavior under a wide range of physical conditions.

The goal of unfolding is to remove the detector response from the data, leaving only the underlying physics. To achieve this, the response matrices are interpolated to provide a continuous, response function for each energy bin. For a given response function $R(e', e, m, q)$ that lies between two known response functions $R(e', e_1, m_1, q_1)$ and $R(e', e_2, m_2, q_2)$; with $e_1 < e < e_2$, $m_1 < m < m_2$, and $q_1 < q < q_2$, a total of 8 response matrices are required for full trilinear interpolation.

To reduce the number of required simulations, weighting factors are applied to interpolate between values of multiplicity and Q-value. For multiplicity, weights are defined as:

$$w_{m_1} = \frac{m_2 - m}{m_2 - m_1}, \quad w_{m_2} = 1 - w_{m_1},$$

so that the interpolated response is:

$$R(e', e_1, m, q_1) = w_{m_1} R(e', e_1, m_1, q_1) + w_{m_2} R(e', e_2, m_2, q_2).$$

A similar process is used to interpolate between q_1 and q_2:

$$w_{q_1} = \frac{q_2 - q}{q_2 - q_1}, \quad w_{q_2} = 1 - w_{q_1},$$

yielding:

$$R(e', e_1, m, q) = w_{q_1} R(e', e_1, m, q_1) + w_{q_2} R(e', e_2, m, q_2).$$

This two-step interpolation reduces the required response functions to just two: $R(e', e_1, m, q)$ and $R(e', e_2, m, q)$, which can then be used to calculate the final interpolated response for the desired energy bin.

In the case of a Q_{β^+} decay, the measured excitation energy e' includes the contribution from positron annihilation, and is related to the true excitation energy e by:

$$e' = e + 2m_e c^2, \text{ where } m_e c^2 \approx 511 \text{ keV}.$$

Therefore, when interpolating between e_1 and e_2, one must consider the shifted sum peaks at $e'_1 = e_1 + 1022$ keV and $e'_2 = e_2 + 1022$ keV. A detailed description of this interpolation procedure can be found in Ref. [106].

6.1.2.1 First Implementation of β^+ Unfolding

Due to the β^+ decay of ^{60}Ga, it was necessary to develop and test an excitation energy-axis unfolding procedure for β^+ decays. To validate this approach, a pseudo-nucleus was simulated using GEANT4 ver. 4.9.5. This artificial β^+-decaying nucleus was assigned a Q_{β^+} value of 2.7 MeV and included excited states at 2.5 MeV and 1.7 MeV. The simulated de-excitation emitted γ-rays with energies E_γ = 2.5 MeV, 1.7 MeV, and 0.8 MeV. The level scheme is shown in the inset of Fig.6.2.

The Oslo matrix resulting from this simulation can be seen in Fig. 6.2. It displays several expected features, including bright horizontal bands at E_x = 2.5 MeV + 1022 keV and E_x = 1.7 MeV + 1022 keV, corresponding to the excited states shifted by the positron annihilation energy. Diagonal bands, indicative of strong transitions to discrete levels, are also present, as well as a bright vertical band at E_γ = 511 keV from annihilation γ-rays.

However, several unexpected features arise due to an energy boost along the E_γ axis. This boost occurs because the 511 keV annihilation γ-rays can, and often do, deposit energy in the same NaI crystal coincidentally with de-excitation γ-rays. This results in the apparent energy of individual γ-rays being artificially increased to E_γ + 511 keV.

This effect introduces two main complications: (1) counts appear in the unphysical region of the Oslo matrix where $E_\gamma > E_x$, and (2) localized clusters of counts arise at energies $E_\gamma < E_x$ where no real γ-transitions exist. Both artifacts impact the extraction of the primary γ-ray matrix, discussed in Sec. 6.1.4.

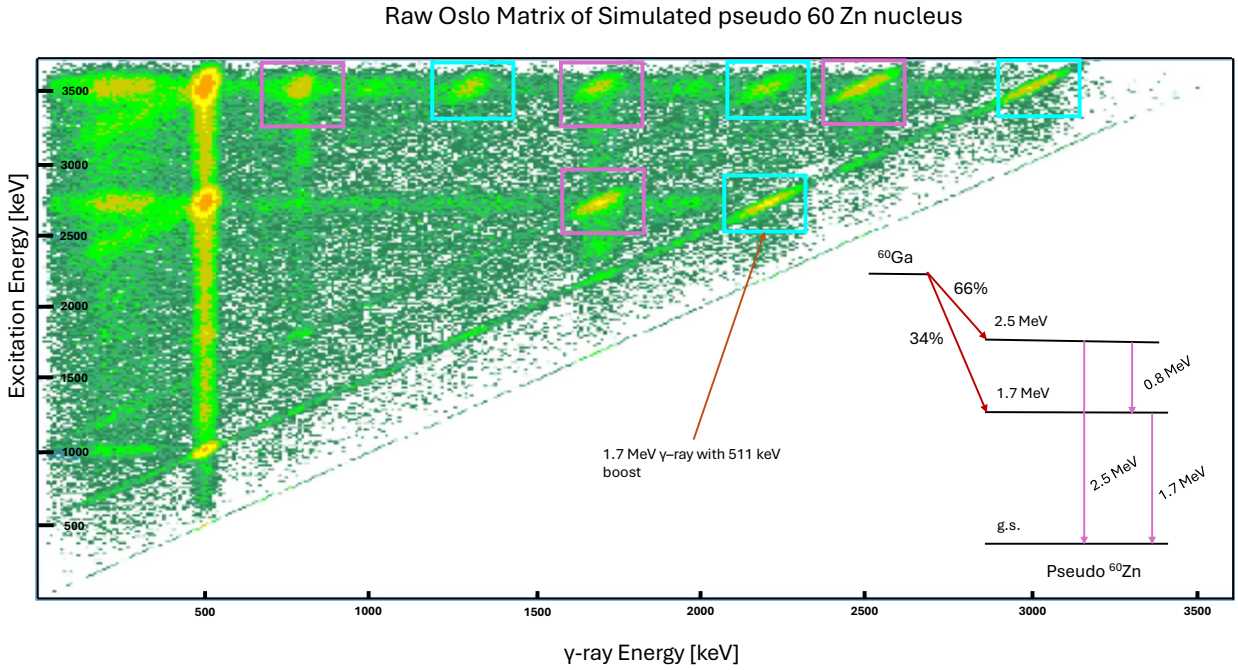

Figure 6.2 Raw matrix of pseudo-nucleus. The regions in purple are the true coincidences from the level scheme. The regions in blue are caused by an annihilation γ-ray entering the same NaI crystal as a de-excitation γ-ray. The inset shows the level scheme of the pseudo nucleus.

6.1.2.2 Folding Iteration Method

The folding iteration method is detailed here [106]; an overview is provided in this subsection. Once an appropriate response function has been determined for all energy bins, we can begin to consider the relationship between the measured spectrum s' and the true spectrum s^0. Assuming there are N energy bins, this relationship can be written as:

$$s' = Rs^0 = \begin{bmatrix} s'_1 \\ s'_2 \\ \vdots \\ s'_N \end{bmatrix} = \begin{bmatrix} R_{11} & \cdots & R_{1N} \\ \vdots & \ddots & \vdots \\ R_{N1} & \cdots & R_{NN} \end{bmatrix} \begin{bmatrix} s_1 \\ s_2 \\ \vdots \\ s_N \end{bmatrix}.$$

In principle, the true spectrum s^0 can be obtained by inverting the response matrix:

$$s^0 = R^{-1}s'.$$

However, this direct inversion approach presents significant challenges. In particular, for large

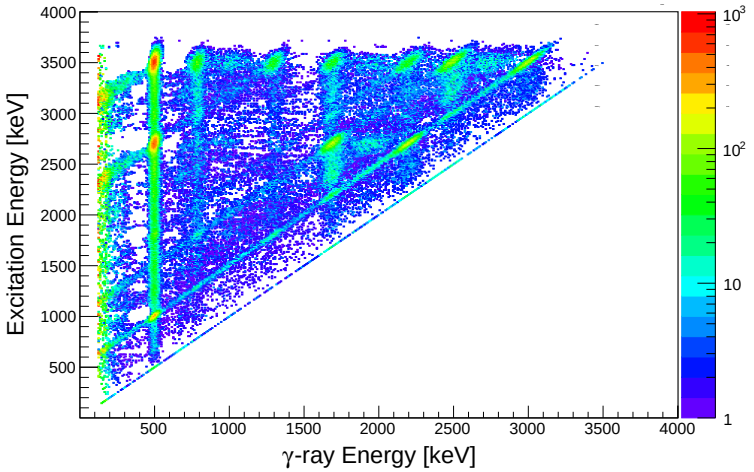

Figure 6.3 γ-ray Energy Unfolding of psuedo-nucleus. Unfolding along this axis retains non-physical structures

N small fluctuations in s' can lead to large, unstable oscillations in the computed s^0. Consequently, this method is numerically unstable and unreliable for practical applications.

To avoid these issues, an iterative folding method is employed to approximate the true spectrum. The process begins by assuming the observed spectrum is the initial estimate of the true spectrum:

$$s^0 = s'.$$

This initial estimate is folded using the response matrix to produce a simulated spectrum:

$$f^0 = Rs^0.$$

The goal is to minimize the difference between the measured spectrum s' and the folded estimate f^0. To improve the approximation, a new estimate of the true spectrum is generated by adding the residual difference to the previous guess:

$$s^1 = s^0 + (s' - f^0).$$

This iterative process continues, with each iteration updating the estimate:

$$s^{i+1} = s^i + (s' - f^i),$$

where $f^i = Rs^i$ is the folded spectrum at iteration i. Iterations are repeated until convergence is achieved, i.e., when $s' \approx f^{(i)}$ within a predefined tolerance. In β^+-decay experiments, an additional preprocessing step is required to reshape the matrix and remove counts from unphysical regions. Specifically, the matrix is truncated such that only counts satisfying the condition $E_x < E_\gamma + \sigma/2$ are retained, where σ is the full width at half maximum (FWHM) of a peak centered at $E_x = E_\gamma$. While some counts may still remain in the unphysical region, preserving the full peak shape is essential for accurate primary γ-ray extraction.

6.1.3 Extraction of Primary γ-rays

Once the detector response has been unfolded from the data matrix, the next step is to extract the primary γ-ray matrix.

To isolate the primary γ-ray matrix, an iterative subtraction method is used. For each excitation energy bin E_{x_i}, a γ-ray spectrum f_i is constructed. The first-generation γ-ray spectrum for the highest excitation bin, $f_{\max}$, is computed by subtracting a weighted sum of all lower f_i spectra [107]:

$$h = f_{\max} - \sum_i n_i w_i f_i,$$

where w_i are the probabilities of decay from the highest bin to bin i, and n_i are normalization coefficients. Since the w_i values are not known, they must be determined iteratively.

Following the method described in Ref. [107], an initial trial set of weights w_{trial} is chosen to calculate a corresponding trial primary spectrum h_{trial}. This spectrum is then unfolded, normalized to an area of 1, and energy-calibrated to match w_{trial}. If the resulting set of weights w_{new} does not match w_{trial} within acceptable uncertainty, the process is repeated with w_{new} until convergence is achieved. Typically, convergence occurs within three iterations.

Using the pseudo-nucleus described in Sec. 6.1.2.1, subtracting the $E_x = 1.7$ MeV bin from the $E_x = 2.5$ MeV bin leaves behind real primary γ-rays at 2.5 MeV and 0.8 MeV, successfully removing the 1.7 MeV component of the cascade. However, boosted peaks at 0.8 + 0.511 MeV, 1.7 + 0.511 MeV, and the 2.5 MeV + 0.511 MeV remain. During this subtraction process, the γ-ray spectra associated with each E_{x_i} bin can exhibit peaks at both E_γ and $E_\gamma + 511$ keV. When

subtracting lower excitation bins from the highest one, boosted peaks may remain. As a result, the primary matrix for this bin contains four γ-ray peaks: two real and two boosted. In this simple case, where boosted peaks are clearly identifiable, they can be corrected by selecting the peaks in the original E_γ histogram and subtracting 0.511 MeV from their energy. However, for real nuclei, this method becomes invalid due to the presence of continuum states, which are characterized by a nuclear level density rather than discrete energy levels—one of the very quantities this method seeks to determine. Thus, it is not currently possible to distinguish whether counts in the continuum arise from true de-excitation γ-rays or from boosted γ-rays. In cases involving direct ground-state transitions, this issue can be mitigated by applying a cut to the primary matrix, effectively removing events with $E_\gamma \approx E_x + 50$ keV. This restores the expected triangular shape of the matrix and excludes the boosted γ-rays from the analysis. The 50 keV value was chosen because it is half of the width of the Ex=$E\gamma$ peak.

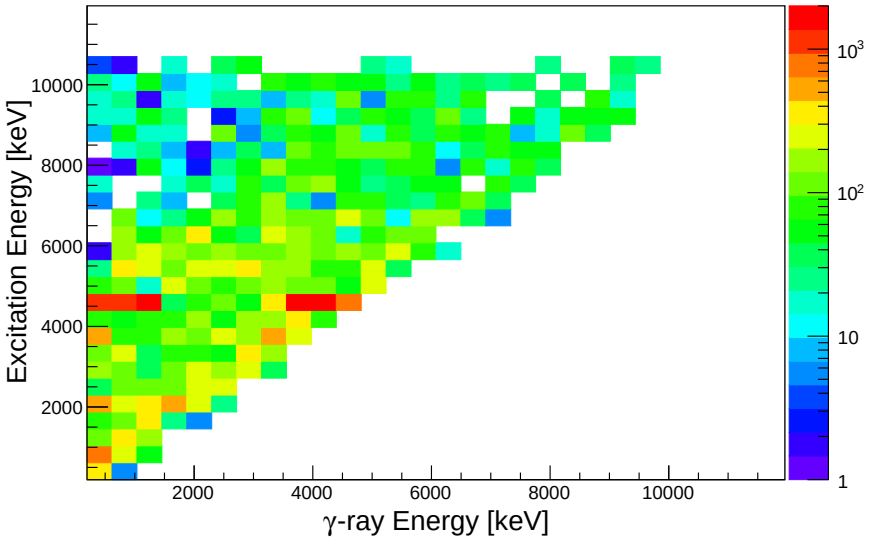

Figure 6.4 Primary γ matrix of ^{60}Zn data after compression. This is the version that will be used in to determine the forms of the NLD and γSF.

Final Matrix Preparation Once all parameters have been determined, the primary γ matrix can be fully extracted. Often, the resulting matrix contains empty bins or sparse regions with insufficient statistics. To mitigate this, it is standard practice to rebin the matrix into larger energy

intervals, with priority given to reducing gaps in the statistical region of the matrix. The extracted experimental primary γ spectra was compressed to 420 keV/bin (Fig. 6.4) due to low statistics

6.1.4 Determining the NLD and γSF

With the primary γ-ray matrix extracted, we can now determine the nuclear level density (NLD) and γ-ray strength function (γSF). This process involves three tools found in the Oslo Method software package [108]: `RhoSigChi`, `Counting`, and `Strength`.

The `RhoSigChi` code is used to define the statistical region of interest in the matrix, input the final bin size, and select the E_γ and E_x energy ranges. Using this information, it extracts the functional forms of both the NLD and transmission coefficients. The `Counting` code then applies user-defined constraints to determine the NLD scaling factor A and the slope parameter α, which is common to both the NLD and the transmission coefficient. Finally, the `Strength` code uses the transmission coefficients and α to determine the scaling factor B, yielding the final normalized form of the γSF.

6.1.4.1 Extracting the Functional Form of NLD and Transmission coefficients [109]

The `RhoSigChi` code assumes that the experimental primary γ-ray matrix $\Gamma(E_x, E_\gamma)$ is normalized such that:

$$\sum_{E_x=E_x^{\min}}^{E_x^{\max}} \Gamma(E_x, E_\gamma) = 1.$$

Under this normalization, $\Gamma(E_x, E_\gamma)$ represents the relative transition probability for a γ decay from an initial excitation energy E_i to a final state at $E_f = E_i - E_\gamma$.

From Fermi's Golden Rule, the transition rate is given by:

$$\lambda_{i\to f} = \frac{2\pi}{\hbar}|\langle f|\hat{H}|i\rangle|^2\rho_f,$$

where $\hat{H}$ is the transition operator and ρ_f is the level density at the final energy. This implies that the primary γ matrix can be factorized as:

$$\Gamma_{\text{th}}(E_x, E_\gamma) \propto T(E_\gamma)\rho(E_x - E_\gamma),$$

where $T(E_\gamma)$ is the transmission coefficient and ρ is the level density. The theoretical matrix must satisfy the same normalization condition as the experimental one:

$$\sum_{E_\gamma = E_\gamma^{\min}}^{E_x} \Gamma_{\text{th}}(E_x, E_\gamma) = 1,$$

leading to the final form:

$$\Gamma_{\text{th}}(E_x, E_\gamma) = \frac{T(E_\gamma)\rho(E_x - E_\gamma)}{\sum_{E_\gamma = E_\gamma^{\min}}^{E_x} T(E_\gamma)\rho(E_x - E_\gamma)}.$$

To extract the functional forms of $T(E_\gamma)$ and $\rho(E_x - E_\gamma)$, a χ^2 minimization is performed over many iterations:

$$\chi^2 = \frac{1}{N_{\text{free}}} \sum_{E_x = E_x^{\min}}^{E_x^{\max}} \sum_{E_\gamma = E_\gamma^{\min}}^{E_x} \left(\frac{\Gamma_{\text{th}}(E_x, E_\gamma) - \Gamma(E_x, E_\gamma)}{\Delta\Gamma(E_x, E_\gamma)} \right)^2,$$

where $\Delta\Gamma(E_x, E_\gamma)$ is the uncertainty on each matrix element, and N_{free} is the number of degrees of freedom. This value is computed by subtracting the number of data points in both T and ρ from the number of data points in the matrix. Full details of the method can be found in [109].

The functional forms of T and ρ are not unique solution of Γ. Any transformation of slope or scale can also lead to a valid outcome as well. The leads to the transformation equations:

$$\tilde{\rho}(E - E_\gamma) = Ae^{\alpha(E - E_\gamma)}\rho(E - E_\gamma)$$

$$\tilde{T}(E_\gamma) = Be^{\alpha(E_\gamma)}T(E_\gamma)$$

The parameters A, B, and α are determined by fitting the functional forms of ρ and T to data through processes described in 6.1.4.2 and 6.1.4.3

6.1.4.2 NLD Normalization

The `Counting` code uses the unnormalized level density output from `RhoSigChi` to determine the transformation parameters A and α. These parameters are used to normalize the level density to known discrete levels at low excitation energies, and at higher energies to resonance spacing data near the neutron separation energy if available or theoretical estimates. In this work, we normalize to a Shell Model calculation presented in [110] at 8 MeV. This energy was chosen because it was just beyond the end of our data and therefore extrapolation to the point would introduce minimal uncertainty. First, the extracted level density is scaled to match the functional form of a chosen

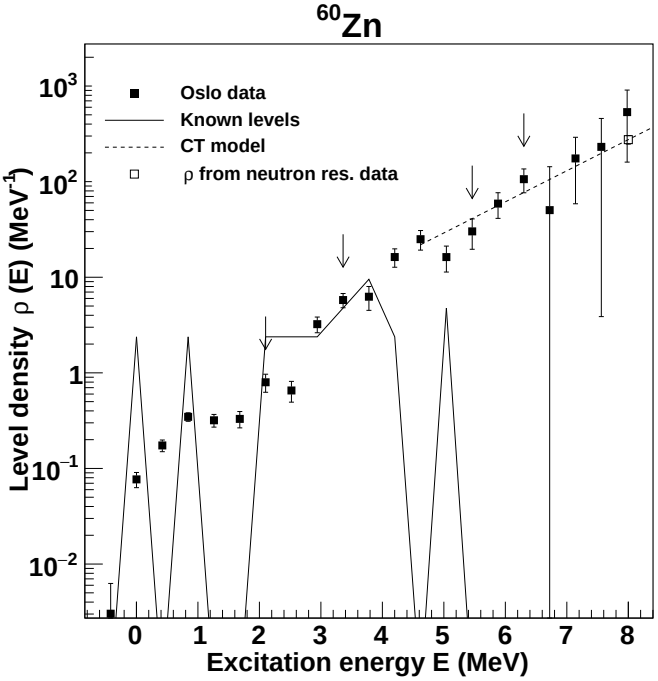

Figure 6.5 NLD output from the Oslo Mehtod

model, such as the Constant Temperature Model (CTM) or the Fermi Gas Model (FGM), by adjusting A and α. The level density is then further scaled to match the known low-energy discrete levels and the high-energy normalization point.

6.1.4.3 γSF Normalization

With α known from the `Counting` procedure, the only remaining free parameter for the γSF is the scaling factor B. In general, B can be determined using the average total radiative width of

s-wave neutron resonances. However, in the case of ^{60}Zn, no such data exists at this time.

As an alternative, an initial estimate for B is obtained by comparing the extracted γSF to known γSF values from neighboring isotopes of similar mass. This provides a reasonable starting point for the final normalization of the strength function.

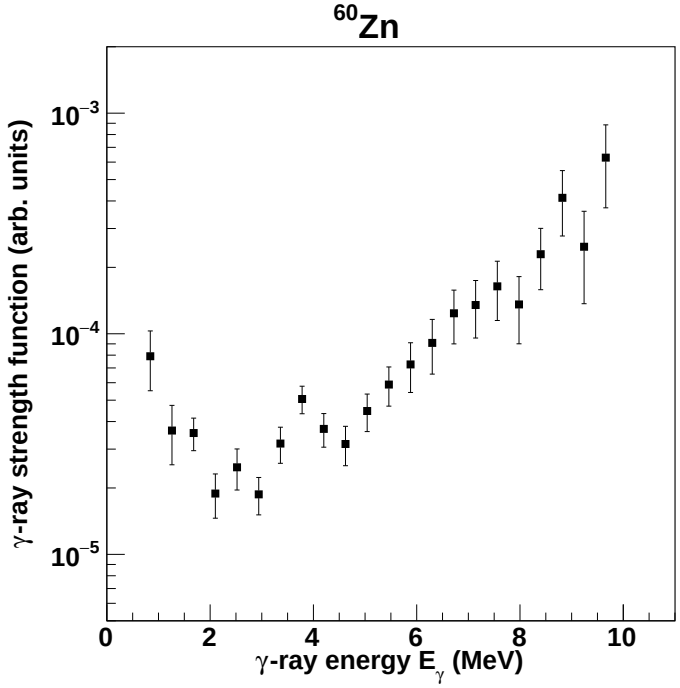

Figure 6.6 Output from the Oslo Method showing the functional form of the γ-ray Strength Function, before scaling to data in mass region

The data was set in 30 keV bins in the 2D matrix.. A reference point of 273 levels was set at 8 MeV calculated from a spin reduction on the shell model prediction for work done by Ohio University [110].

The raw γSF extracted from the Oslo Method is not normalized, so the data must be scaled to experimental results of nearby nuclei. The ^{60}Zn γSF was scaled to Oslo method data from ^{56}Fe [111] between 4-9 MeV. After scaling, the experimental γSF is consistent with γSF data from near mass nuclei 6.7.

Once the γSF and NLD were extracted, the TALYS they were fit to TALYS models using an Adaptive Multi Chain Monte Carlo (MCMC) Bayesian analysis to extract model parameters.

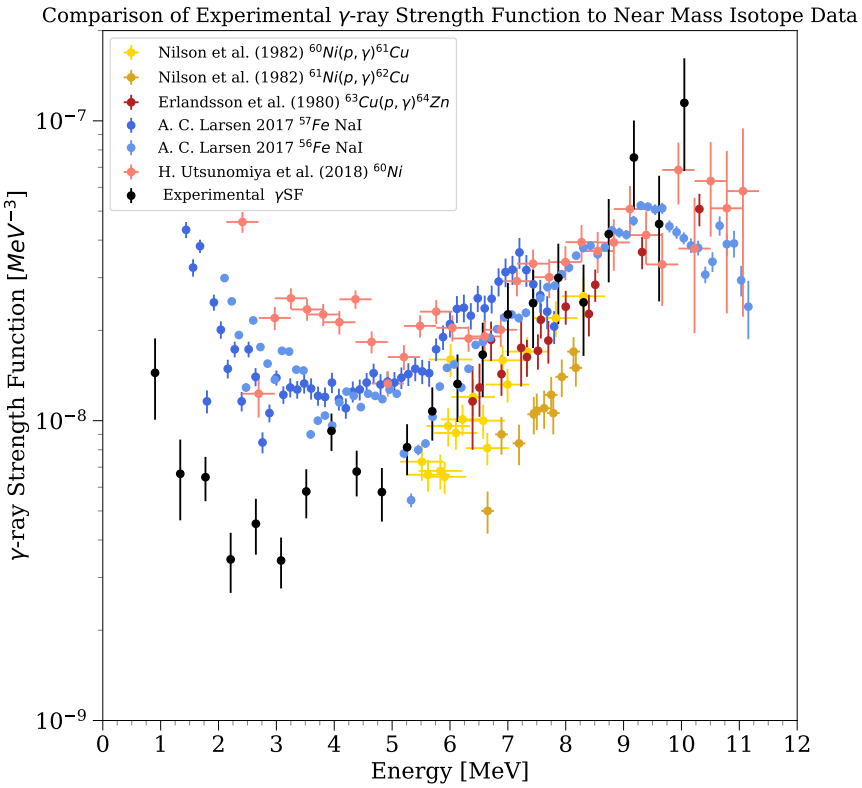

Figure 6.7 Comparison of Experimental γ-ray Strength Function to available data in mass region. Experimental data was scaled to A.C. Larsen (2017) [111] with a factor of 1.8262×10^{-4}. The other datasets are from Nilson [112], Erlandsson [113], and Utsunomiya [114].

6.2 Bayesian Inference Tools for Error Determination

Bayesian inference is a statistical framework for estimating probable parameter values given a data set and prior knowledge. Formally Bayes' Theorem is [115]

$$P(\theta|D,M) = \frac{P(D|\theta,M)P(\theta|M)}{P(D|M)} = \frac{Likelihood\ Prior}{Evidence}$$

where D is the experimental data, M is the model used to describe the data, and θ is the parameter set used in the model. In this work, Bayesian inference is used in the development of a computational tool, used to determine parameters of models in TALYS that fit the NLD and γSF data, within 95% and 68% ($\approx 2\sigma$ and 1σ respectively for Gaussian data) credible intervals(CIs).

Prior $P(\theta|M)$ The prior encompasses any additional information beyond the data. It is a probability density that represents the degree of belief that the parameter lies within a given interval before the data are observed [116]. The prior assumed a gaussian distribution for the parameters and

contained information about the parameter limits from the TALYS manual [29]. Parameter limits must be clearly defined as the code can converge to many different unphysical solutions outside the bounds of what TALYS allows. Both the NLD and γSF priors apply a Heaviside function to the parameters, keeping them within the model bounds.

Likelihood $P(D|\theta, M)$ The Likelihood is a function proportional to the probability that the data is observed given the model with the specified parameter values. The likelihood function used a χ^2 minimization for a log likelihood. Log likelihood improves numerical stability because exponentiating large χ^2 values can lead to numerical overflow.

Model evidence $P(D|M)$ The model evidence is the probability to observe the data given the model, averaging over the entire parameter space [116]

$$P(D|M) = \int P(D|\theta, M)P(\theta, M)d\theta$$

This variable describes how well a model generally describes the data and is mainly used to compare models against each other. As model comparisons are beyond the scope of this project, the evidence acts as a normalization constant and does not need to be computed explicitly.

Posterior $P(\theta|D, M)$ The posterior is the conditional probability distribution of the model parameters, given the data [116]. Once sampled, the parameters visited were used in TALYS to infer the cross section of the $^{59}Cu(p,\gamma)^{60}Zn$ reaction.
It is important to note that the use of log likelihood implies the use of a log prior and results in a log posterior. This log posterior is then exponentiated for the true posterior distribution. For more details see the appendix .

6.2.1 Metropolis-Hastings Algorithm

To implement Bayesian inference on the models and data, a random walk Monte Carlo method was used with the Metropolis-Hastings (MH) algorithm. This algorithm has been used successfully since its origin at Los Alamos National Laboratory in the 1940s and 1950 [117]. MH is one of many

algorithms used for parameter searches. The key inputs of the algorithm are: number of calculation steps, step size, and initial parameter guesses. The algorithm first calculates the log prior and log likelihood of the initial parameter guesses. Once the log likelihood and log prior are calculated, their sum is used to calculate the log posterior distribution log(P(Y|α)). The algorithm will hold this in a separate variable, called current posterior for the initial guess. For every subsequent step, new parameters are proposed. These proposed parameter guesses are used to determine a proposed posterior. To determine whether the proposed step is taken or not, an acceptance probability is calculated from the the proposed and current log posteriors.

$$P_{Accept} = min(1, exp(log(p) - log(c))$$

A randomly generated value between (0,1] from a uniform distribution is compared to the acceptance probability. If the random number is less than P_{accept}, the step is accepted, and the proposed posterior replaces the current posterior; otherwise, it is rejected, and the current posterior remains. This process occurs in two phases, burn (thermalization) and calculation. In the burn phase, the algorithm takes a user defined number of steps to move away from the initial guess without recording the accepted posterior. While not an explicitly necessary step of the Metropolis-Hastings algorithm, the burn phase is useful to ensure that the results are not biased by the initial guess. In the calculation phase, accepted steps are recorded, and the number of acceptances is compared with the total number of calculation steps to create an acceptance ratio.

6.2.2 Comparison to data

In order to compare the parameter distributions found by the Metropolis-Hastings algorithm to the data, first the total accepted parameter set is randomly sampled. All of the parameters in the sample are then used to generate a subset of models. The 50th percentile model is used as the median prediction of the Bayesian calculation, the 95% CI is determined by the region bounded by the 2.5 and 97.5 percentile models,and the 68% CI is determined by the region bounded by the 16 and 84 percentile models. The median prediction and CI are plotted on top of the full experimental data set, as well as the subset of data used for the Bayesian calculation.

6.3 Nuclear Level Density and γ-ray Strength Function

TALYS level density model 5 [118] was fit to the experimental NLD to account for an uneven parity distribution. The γSF was fit to strength model 10, Skryme HFB + QRPA [17] with a low energy enhancement model found in the TALYS 2.0 manual [29]. The NLD was fit from 3 to 10 MeV using the ctable and ptable parameters. The γSF was fit from 0 to 10 MeV with the parameters Etable, ftable, wtable for the E1 component and updende, upbendc, upbendf, and beta2 for the M1 low energy enhancement. The base M1 component was modeled with the default option, spin-flip with scissors mode.

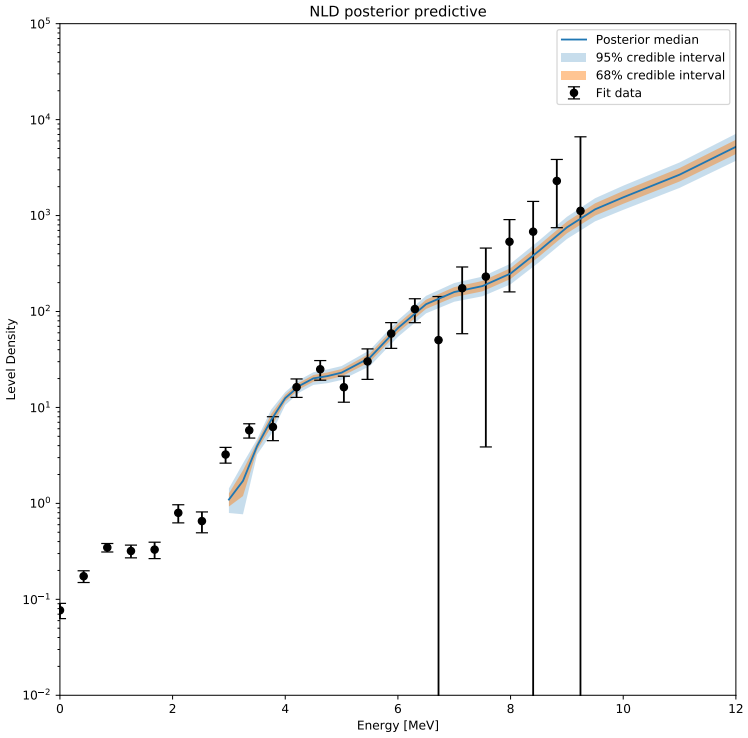

Figure 6.8 Fit of Nuclear Level Density data to level density model 5 in TALYS. The median parameter values are: ctable - -0.076 ; ptable - 2.40 The best fit parameters are : ctable - -0.06 ; ptable - 2.41

The final fits are presented in Fig.6.8 and 6.9 for the NLD and γSF respectively. The NLD and γSF pilot runs had a burn phase of 10 000 steps and recorded 20 000 steps. The production runs

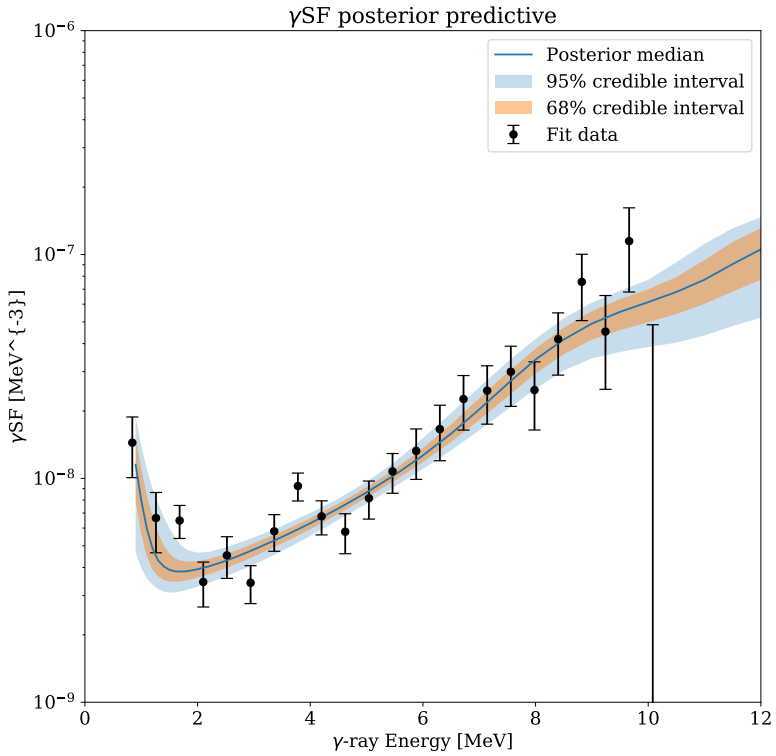

Figure 6.9 Fit of experimental γSF to TALYS strength model 10 with M1 model 3 and the low energy enhancement model. The data and fit are compared to γSF data from near mass nuclei. The median parameters the best fit parameters are: wtable- 9.483e-1, Etable - 8.99e-1,ftable - 3.10e-1, upbendc - 1.20e-06, upbende 1.96, upbendf - 2.29,beta2 - 1.3

used a burn of 20 000 and recorded for 50 000 steps. The resulting posterior parameter distribution described the combinations of model parameters that best reproduce the experimental NLD and γSF data. The NLD posterior ESS (Appendix. .2) was »> for ctable and ptable respectively. The γSF posterior ESS was . These ESS are all high (> 1000) showing that the model explored the parameter space effectively. There is excellent agreement for both, especially in the statical region where these functions are most relevant in Hauser-Feshback calculations. The low energy enhancement in the γSF is also reproduced well.

6.4 Extraction of Cross Section and Reaction Rate

The posterior parameters that created the CI bands were sampled and used to create 8000 TALYS input files. Each file randomly pairs the sampled NLD and γSF parameter sets. The cross

section and astrophysical reaction rate calculations from TALYS are used to create new CI bands. These CI bands are compared to a default TALYS band. This default band is constructed from every combination of level density 2.2 and γ strength 2.3 models using default parameters for all. Although the data was fit only with strength model 10 [17], the results are model independent as

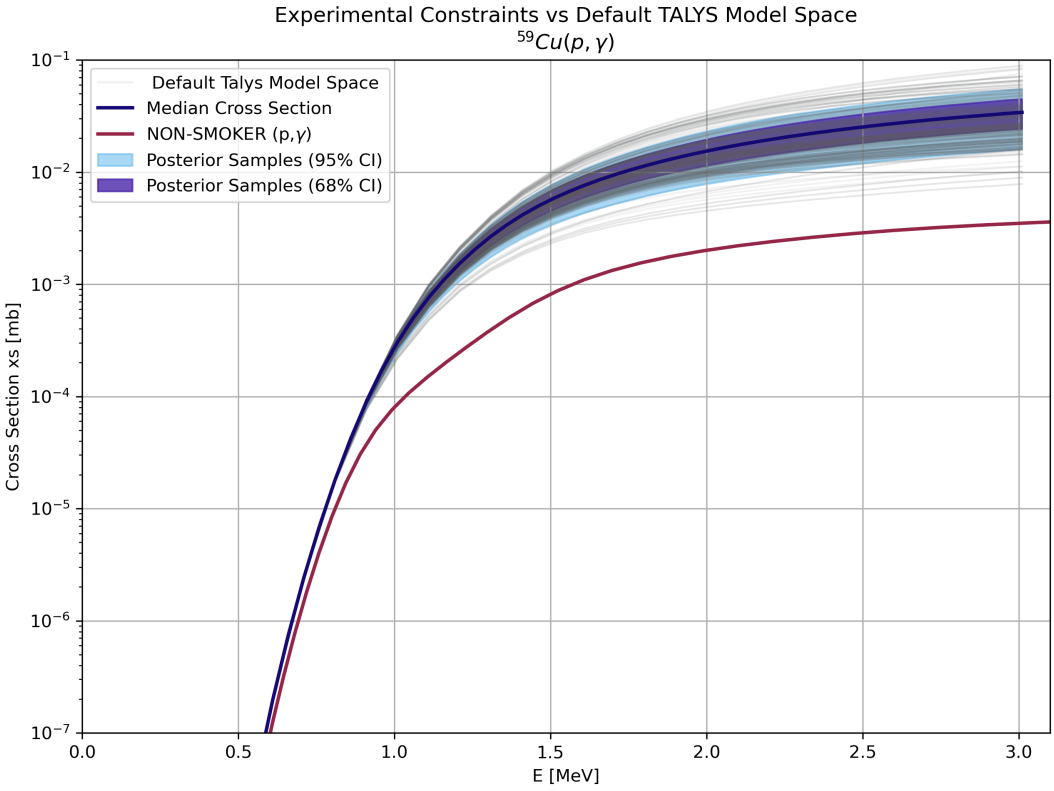

Figure 6.10 Calculated Cross Section from fits compared with default TALYS parameters (gray) and NONSMOKER [119](red) calculations. The wide default TALYS range is constrained well by both CI regions. The consistent disagreement with NON-SMOKER suggests underlying model differences.

the parameters shaped the model to the data. The TALYS cross section uncertainty, Fig.6.10, is constrained by a factor of approximately 4.6 at 3 MeV and the reaction rate, Fig.6.11 by around 2.5 and 2.5 GK . Interestingly, TALYS suggests the $^{59}Cu(p,\gamma)$ channel is much stronger than any other potential exit channel. REACLIB [120] and NON-SMOKER [119] both show a competition between (p,γ) and (p,α) channels. The source of this discrepancy is unclear. Taken at face value, the TALYS cross section and reaction rate derived from experimental data suggest that there is

no NiCu cycle in the rp-process temperture range of 0.4-1.1 GK. Instead the reaction path flows upward on the chart of nuclides through the (p,γ) channel. The νp process will see contributions from NiCu for CCSN temperatures >3GK, where the (p,α) reaction rate is roughly 10% of the experimental median (p,γ) rate. Once the ejected material cools past this temperature, shifting the reaction flow into the ^{60}Zn waiting point.

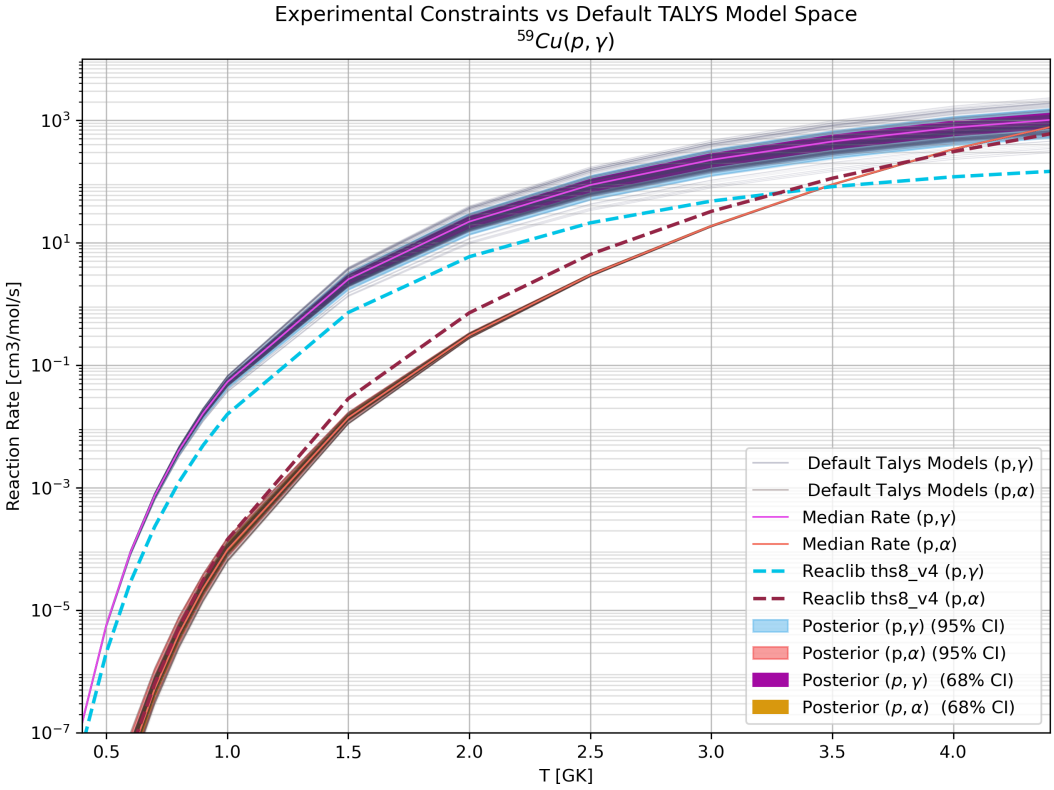

Figure 6.11 Astrophysical reaction rate from fits compared with default TALYS parameters and REACLIB [120]. The (p,α) reaction is plotted to show channel competition. No constraint is made on the (p,α) channel.

CHAPTER 7

CONCLUSION

This thesis aimed to determine the I_β of ^{60}Ga, as well as the NLD and γSF of ^{60}Zn, a key isotope in the rapid proton and neutrino proton capture processes, through the total absorption spectroscopy and β^+Oslo methods. Whereas the TAS technique has been well established in the literature; the β^+ Oslo technique is described for the first time, along with tests of its capabilities. Also, a novel (to this application) adaptive Bayesian statistical parameter determination tool was developed for an in depth uncertainty analysis.

The key result of the TAS analysis is the 12.8% feeding above the proton separation energy, higher than predictions from both the GXPF1A and K3BG shell model hamiltonians. The GXPF1A hamiltionian agrees well with the experimental I_β and B(GT); however, the other models used show significant deviation. The half-life was calculated as 57.7±9.8 ms, in agreement with previous experimental measurements, the GXPF1A hamiltonian (64 ms), and the DC3* QRPA parameterization for the meson-nucleon Lagrangian (58.3 ms).

In chapter 6.1, the excitation unfolding method is described for the first time. Testing showed that, while artifacts remain, the extracted NLD and γSF are still reasonable. Also for the first time, the excitation unfolding was included in the full β Oslo pipeline to extract NLD and γSF from a proton rich isotope. The extracted level density from this work disagrees with the experimental result in [121], as this result did not produce a reasonable γSF within the β^+ Oslo method.

The experimental γSF and NLD from this work were fit to TALYS level density model 5 and strength model 10 using an adaptive multi chain monte carlo Bayesian statistical tool. This tool uses a two stage approach to map out the parameter space for more accurate determination of best fit parameters. 8 000 parameter samples from both the NLD and γSF fit were randomly paired and input into TALYS to calculate the (p,γ) reaction cross section and astrophysical reaction rate. The resulting confidence intervals constrain the TALYS cross section uncertainty by roughly a factor of 4.6 at 3 MeV and the reaction rate is constrained by around 2.5 at 2.5 GK. Comparing the experimental (p,γ) CI with (p,α) predictions from REACLIB and NON-SMOKER shows that the

two channels do not meaningfully compete until >4 GK, well above the maximum temperatures for both the rp and νp processes. The data is also compared to $^{59}Cu(p,\alpha)$ from Lopez-Saavedra et al. [122], illustrating an even higher competition temperature. With this evidence in mind, we conclude that the NiCu cycle is an unlikely path for the rapid proton capture and neutrino proton capture processes, instead the reaction path flows up the chart of nuclides to heavier mass isotopes.

BIBLIOGRAPHY

[1] E. Rutherford, "Lxxix. the scattering of α and β particles by matter and the structure of the atom," *The London, Edinburgh, and Dublin Philosophical Magazine and Journal of Science*, vol. 21, no. 125, pp. 669–688, 1911.

[2] A. S. Eddington, "The internal constitution of the stars," *The Scientific Monthly*, vol. 11, no. 4, pp. 297–303, 1920.

[3] G. LEMAÎTRE, "The beginning of the world from the point of view of quantum theory," *Nature*, vol. 127, pp. 706–706, May 1931.

[4] E. M. Burbidge, G. R. Burbidge, W. A. Fowler, and F. Hoyle, "Synthesis of the elements in stars," *Rev. Mod. Phys.*, vol. 29, pp. 547–650, Oct 1957.

[5] M. Arnould and S. Goriely, "The p-process of stellar nucleosynthesis: astrophysics and nuclear physics status," *Physics Reports*, vol. 384, no. 1, pp. 1–84, 2003.

[6] A. Koning, S. Hilaire, and S. Goriely, "TALYS: modeling of nuclear reactions," *The European Physical Journal A*, vol. 59, p. 131, 2023.

[7] C. Illiadis, *Nuclear Physics of Stars*. John Wiley & Sons, Ltd, 2007.

[8] J. Suhonen, *From Nucleons to Nucleus: Concepts of Microscopic Nuclear Theory*. Theoretical and Mathematical Physics, Berlin, Germany: Springer, 2007.

[9] S. Navas, C. Amsler, T. Gutsche, C. Hanhart, J. J. Hernández-Rey, and et.al, "Review of particle physics," *Phys. Rev. D*, vol. 110, p. 030001, Aug 2024.

[10] J. Liu, M. P. Mendenhall, A. T. Holley, H. O. Back, T. J. Bowles, and et.al, "Determination of the axial-vector weak coupling constant with ultracold neutrons," *Phys. Rev. Lett.*, vol. 105, p. 181803, Oct 2010.

[11] I. S. Towner and J. C. Hardy, "The evaluation of vud and its impact on the unitarity of the cabibbo–kobayashi–maskawa quark-mixing matrix," *Reports on Progress in Physics*, vol. 73, p. 046301, mar 2010.

[12] F. Osterfeld, "Nuclear spin and isospin excitations," *Rev. Mod. Phys.*, vol. 64, pp. 491–557, Apr 1992.

[13] M. G. Mayer and J. H. D. Jensen, *Elementary Theory of Nuclear Shell Structure*. New York: John Wiley & Sons, Inc., 1955.

[14] C. Mahaux and H. A. Weidenmueller, *SHELL-MODEL APPROACH TO NUCLEAR REACTIONS*. North-Holland, 01 1969.

[15] E. Caurier, G. Martínez-Pinedo, F. Nowacki, A. Poves, and A. P. Zuker, "The shell model as a unified view of nuclear structure," *Rev. Mod. Phys.*, vol. 77, pp. 427–488, Jun 2005.

[16] P. Ring and P. Schuck, *The Nuclear Many-Body Problem*. Theoretical and Mathematical Physics, Springer Berlin Heidelberg, 2004.

[17] S. Goriely, E. Khan, and M. Samyn, "Microscopic hfb + qrpa predictions of dipole strength for astrophysics applications," *Nuclear Physics A*, vol. 739, no. 3, pp. 331–352, 2004.

[18] A. Larsen, A. Spyrou, S. Liddick, and M. Guttormsen, "Novel techniques for constraining neutron-capture rates relevant for r-process heavy-element nucleosynthesis," *Progress in Particle and Nuclear Physics*, vol. 107, pp. 69–108, 2019.

[19] N. BOHR, R. PEIERLS, and G. PLACZEK, "Nuclear reactions in the continuous energy region," *Nature*, vol. 144, pp. 200–201, Jul 1939.

[20] T. Rauscher and F.-K. Thielemann, "Astrophysical reaction rates from statistical model calculations," *Atomic Data and Nuclear Data Tables*, vol. 75, no. 1, pp. 1–351, 2000.

[21] A. Koning and J. Delaroche, "Local and global nucleon optical models from 1 kev to 200 mev," *Nuclear Physics A*, vol. 713, no. 3, pp. 231–310, 2003.

[22] J.-P. Jeukenne, A. Lejeune, and C. Mahaux, "Optical-model potential in finite nuclei from reid's hard core interaction," *Phys. Rev. C*, vol. 16, pp. 80–96, Jul 1977.

[23] B. V. Carlson, "The optical model." Lectures presented at the ICTP Workshop on Nuclear Structure and Decay Data, May 2010.

[24] T. Ericson, "The statistical model and nuclear level densities," *Advances in Physics*, vol. 9, no. 36, pp. 425–511, 1960.

[25] L. Kirsch and L. Bernstein, "Rainier: A simulation tool for distributions of excited nuclear states and cascade fluctuations," *Nuclear Instruments and Methods in Physics Research Section A: Accelerators, Spectrometers, Detectors and Associated Equipment*, vol. 892, pp. 30–40, 2018.

[26] S. M. Grimes, J. D. Anderson, J. W. McClure, B. A. Pohl, and C. Wong, "Level density and spin cutoff parameters from continuum (p, n) and (α, n) spectra," *Phys. Rev. C*, vol. 10, pp. 2373–2386, Dec 1974.

[27] S. I. Al-Quraishi, S. M. Grimes, T. N. Massey, and D. A. Resler, "Level densities for $20 < a < 110$," *Phys. Rev. C*, vol. 67, p. 015803, Jan 2003.

[28] S. Goriely, S. Hilaire, and A. J. Koning, "Improved microscopic nuclear level densities within the hartree-fock-bogoliubov plus combinatorial method," *Phys. Rev. C*, vol. 78, p. 064307, Dec 2008.

[29] A. Koning, S. Hilaire, and S. Goriely, "TALYS-2.0: A Nuclear Reaction Program, User Manual." `https://nds.iaea.org/talys/tutorials/talys.pdf`, 2023. International Atomic Energy Agency Nuclear Data Services TALYS tutorial.

[30] A. Gilbert and A. G. W. Cameron, "A composite nuclear-level density formula with shell corrections," *Canadian Journal of Physics*, vol. 43, no. 8, pp. 1446–1496, 1965.

[31] W. Dilg, W. Schantl, H. Vonach, and M. Uhl, "Level density parameters for the back-shifted fermi gas model in the mass range $40 < a < 250$," *Nuclear Physics. A*, vol. 217, 12 1973.

[32] A. Ignatyuk, K. Istekov, G. Smirenkin, and F. Kernforschungszentrum Karlsruhe G.m.b.H. (Germany, "Role of collective effects in systematics of level density of nuclei," *Sov. J. Nucl. Phys.*, vol. 29, Oct 1979.

[33] A. V. Ignatyuk, J. L. Weil, S. Raman, and S. Kahane, "Density of discrete levels in ^{116}Sn," *Phys. Rev. C*, vol. 47, pp. 1504–1513, 1993.

[34] S. Goriely, F. Tondeur, and J. Pearson, "A Hartree–Fock Nuclear Mass Table," *Atomic Data and Nuclear Data Tables*, vol. 77, no. 2, pp. 311–381, 2001.

[35] S. Goriely, S. Hilaire, and A. J. Koning, "Improved microscopic nuclear level densities within the Hartree-Fock-Bogoliubov plus combinatorial method," *Phys. Rev. C*, vol. 78, p. 064307, 2008.

[36] S. Hilaire, M. Girod, S. Goriely, and A. J. Koning, "Temperature-dependent combinatorial level densities with the D1M Gogny force," *Phys. Rev. C*, vol. 86, p. 064317, 2012.

[37] D. Brink, *Some aspects of the interaction of light with matter*. University of Oxford, 1955.

[38] P. Axel, "Electric dipole ground-state transition width strength function and 7-mev photon interactions," *Phys. Rev.*, vol. 126, pp. 671–683, Apr 1962.

[39] J. Kopecky, "Gamma-ray strength functions," Aug 1998.

[40] J. Kopecky and M. Uhl, "Test of gamma-ray strength functions in nuclear reaction model calculations," *Phys. Rev. C*, vol. 41, pp. 1941–1955, 1990.

[41] D. Brink, "Individual particle and collective aspects of the nuclear photoeffect," *Nuclear Physics*, vol. 4, pp. 215–220, 1957.

[42] P. Axel, "Electric Dipole Ground-State Transition Width Strength Function and 7-MeV Photon Interactions," *Phys. Rev.*, vol. 126, pp. 671–683, 1962.

[43] S. Goriely and E. Khan, "Large-scale QRPA calculation of E1-strength and its impact on the neutron capture cross section," *Nuclear Physics A*, vol. 706, no. 1, pp. 217–232, 2002.

[44] S. Goriely, E. Khan, and M. Samyn, "Microscopic HFB + QRPA predictions of dipole strength for astrophysics applications," *Nuclear Physics A*, vol. 739, no. 3, pp. 331–352, 2004.

[45] S. Goriely, "Radiative neutron captures by neutron-rich nuclei and the r-process nucleosynthesis," *Physics Letters B*, vol. 436, no. 1, pp. 10–18, 1998.

[46] I. Daoutidis and S. Goriely, "Large-scale continuum random-phase approximation predictions of dipole strength for astrophysical applications," *Phys. Rev. C*, vol. 86, p. 034328, 2012.

[47] S. Goriely, S. Hilaire, S. Péru, and K. Sieja, "Gogny-HFB+QRPA dipole strength function and its application to radiative nucleon capture cross section," *Phys. Rev. C*, vol. 98, p. 014327, 2018.

[48] V. Plujko, O. Gorbachenko, R. Capote, and P. Dimitriou, "Giant dipole resonance parameters of ground-state photoabsorption: Experimental values with uncertainties," *Atomic Data and Nuclear Data Tables*, vol. 123-124, pp. 1–85, 2018.

[49] R. Capote, M. Herman, P. Obložinský, P. Young, S. Goriely, T. Belgya, A. Ignatyuk, A. Koning, S. Hilaire, V. Plujko, and *et al.*, "RIPL – Reference Input Parameter Library for Calculation of Nuclear Reactions and Nuclear Data Evaluations," *Nuclear Data Sheets*, vol. 110, no. 12, pp. 3107–3214, 2009. Special Issue on Nuclear Reaction Data.

[50] N. L. Iudice and F. Palumbo, "New Isovector Collective Modes in Deformed Nuclei," *Phys. Rev. Lett.*, vol. 41, pp. 1532–1534, 1978.

[51] D. Bohle, A. Richter, W. Steffen, A. Dieperink, N. Lo Iudice, F. Palumbo, and O. Scholten, "New magnetic dipole excitation mode studied in the heavy deformed nucleus ^{156}Gd by inelastic electron scattering," *Physics Letters B*, vol. 137, no. 1, pp. 27–31, 1984.

[52] K. Heyde, P. von Neumann-Cosel, and A. Richter, "Magnetic dipole excitations in nuclei: Elementary modes of nucleonic motion," *Rev. Mod. Phys.*, vol. 82, pp. 2365–2419, 2010.

[53] A. Simon, M. Guttormsen, A. C. Larsen, C. W. Beausang, P. Humby, J. T. Harke, R. J. Casperson, R. O. Hughes, T. J. Ross, J. M. Allmond, and *et al.*, "First observation of low-energy γ-ray enhancement in the rare-earth region," *Phys. Rev. C*, vol. 93, p. 034303, 2016.

[54] A. Voinov, E. Algin, U. Agvaanluvsan, T. Belgya, R. Chankova, M. Guttormsen, G. E. Mitchell, J. Rekstad, A. Schiller, and S. Siem, "Large Enhancement of Radiative Strength for Soft Transitions in the Quasicontinuum," *Phys. Rev. Lett.*, vol. 93, p. 142504, 2004.

[55] A. C. Larsen and S. Goriely, "Impact of a low-energy enhancement in the γ-ray strength function on the neutron-capture cross section," *Phys. Rev. C*, vol. 82, p. 014318, 2010.

[56] M. Guttormsen, K. O. Ay, M. Ozgur, E. Algin, A. C. Larsen, F. L. Bello Garrote, H. C. Berg, L. Crespo Campo, T. Dahl-Jacobsen, F. W. Furmyr, and *et al.*, "Evolution of the γ-ray strength function in neodymium isotopes," *Phys. Rev. C*, vol. 106, p. 034314, 2022.

[57] H. Sasaki, T. Kawano, and I. Stetcu, "Quasiparticle random-phase approximation calculations for $m1$ transitions with the noniterative finite-amplitude method and application to neutron radiative capture cross sections," *Phys. Rev. C*, vol. 107, p. 054312, May 2023.

[58] M. Guttormsen, K. O. Ay, M. Ozgur, E. Algin, A. C. Larsen, F. L. Bello Garrote, H. C. Berg, and et.al, "Evolution of the γ-ray strength function in neodymium isotopes," *Phys. Rev. C*, vol. 106, p. 034314, Sep 2022.

[59] E. K. Ronning, *Probing statistical nuclear properties, the Brink-Axel hypothesis, and astrophysical nucleosynthesis processes with ground and isomeric states in ^{70}Cu*. PhD thesis, Michigan State University, 2025.

[60] B. Ryden, *Introduction to Cosmology*. Cambridge University Press, 2 ed., 2016.

[61] D. Baumann, *Cosmology*. Cambridge University Press, 2022.

[62] D. N. Schramm and M. S. Turner, "Big-bang nucleosynthesis enters the precision era," *Rev. Mod. Phys.*, vol. 70, pp. 303–318, Jan 1998.

[63] S. Stahler, F. Shu, and R. Taam, "The evolution of protostars. i - global formulation and results," *The Astrophysical Journal*, vol. 241, pp. 637–654, 09 1980.

[64] F. C. Adams and G. Laughlin, "A dying universe: the long-term fate and evolutionof astrophysical objects," *Rev. Mod. Phys.*, vol. 69, pp. 337–372, Apr 1997.

[65] B. Lazareff, J. Audouze, S. Starrfield, and J. W. Truran, "Hot CNO-Ne cycle hydrogen burning: explosive hydrogen burning in novae.," *ApJ.*, vol. 228, pp. 875–880, Mar. 1979.

[66] F. Hoyle, "On Nuclear Reactions Occuring in Very Hot STARS.I. the Synthesis of Elements from Carbon to Nickel.," *ApJS*, vol. 1, p. 121, Sept. 1954.

[67] P. W. Merrill, "Spectroscopic Observations of Stars of Class S," *apj*, vol. 116, p. 21, July 1952.

[68] D. Watson, C. J. Hansen, J. Selsing, A. Koch, D. B. Malesani, A. C. Andersen, J. P. U. Fynbo, A. Arcones, A. Bauswein, S. Covino, A. Grado, K. E. Heintz, L. Hunt, C. Kouveliotou, G. Leloudas, A. J. Levan, P. Mazzali, and E. Pian, "Identification of strontium in the merger of two neutron stars," *Nature*, vol. 574, pp. 497–500, Oct 2019.

[69] D. Kasen, B. Metzger, J. Barnes, E. Quataert, and E. Ramirez-Ruiz, "Origin of the heavy elements in binary neutron-star mergers from a gravitational-wave event," *Nature*, vol. 551, pp. 80–84, Nov 2017.

[70] A. Tsantiri, *Proton-Capture Cross-Section Measurements for the Astrophysical Gamma Process: From Stable to Radioactive Ion Beams*. PhD thesis, Michigan State University, 2025.

[71] M. Wiedeking, S. Goriely, M. Guttormsen, F. Herwig, A.-C. Larsen, S. N. Liddick, D. Mücher, A. L. Richard, S. Siem, and A. Spyrou, "Unlocking i-process nucleosynthesis by bridging stellar and nuclear physics," *Nature Reviews Physics*, vol. 7, pp. 696–712, Dec 2025.

[72] W. H. G. Lewin, J. van Paradijs, and R. E. Taam, "X-Ray Bursts," *ssr*, vol. 62, pp. 223–389, Sept. 1993.

[73] C. Fröhlich, G. Martínez-Pinedo, M. Liebendörfer, F.-K. Thielemann, E. Bravo, W. R. Hix, K. Langanke, and N. T. Zinner, "Neutrino-induced nucleosynthesis of $a\>64$ nuclei: The νp process," *Phys. Rev. Lett.*, vol. 96, p. 142502, Apr 2006.

[74] Z. Meisel, A. Deibel, L. Keek, P. Shternin, and J. Elfritz, "Nuclear physics of the outer layers of accreting neutron stars," *Journal of Physics G: Nuclear and Particle Physics*, vol. 45, p. 093001, jul 2018.

[75] A. E. Champagne and M. Wiescher, "Explosive hydrogen burning," *Annual Review of Nuclear and Particle Science*, vol. 42, pp. 39–76, Jan. 1992.

[76] R. K. Wallace and S. E. Woosley, "Explosive hydrogen burning," *apjs*, vol. 45, pp. 389–420, Feb. 1981.

[77] H. Schatz, A. Aprahamian, V. Barnard, L. Bildsten, A. Cumming, M. Ouellette, T. Rauscher, F.-K. Thielemann, and M. Wiescher, "End point of the *rp* process on accreting neutron stars," *Phys. Rev. Lett.*, vol. 86, pp. 3471–3474, Apr 2001.

[78] Buras, R., Rampp, M., Janka, H.-Th., and Kifonidis, K., "Two-dimensional hydrodynamic core-collapse supernova simulations with spectral neutrino transport - i. numerical method and results for a $15m_{\odot}$ star," *A&A*, vol. 447, no. 3, pp. 1049–1092, 2006.

[79] A. Arcones, C. Fröhlich, and G. Martínez-Pinedo, "Impact of supernova dynamics on the νp-process," *The Astrophysical Journal*, vol. 750, p. 18, apr 2012.

[80] F.-K. Thielemann, I. Dillmann, K. Farouqi, T. Fischer, C. Fröhlich, A. Kelic-Heil, I. Korneev, K.-L. Kratz, K. Langanke, M. Liebendörfer, I. V. Panov, G. Martinez-Pinedo, and T. Rauscher, "The r-, p-, and νp-process," *Journal of Physics: Conference Series*, vol. 202, p. 012006, jan 2010.

[81] J. S. Randhawa, R. Kanungo, J. Refsgaard, P. Mohr, T. Ahn, M. Alcorta, C. Andreoiu, S. S. Bhattacharjee, B. Davids, G. Christian, A. A. Chen, R. Coleman, P. E. Garrett, G. F. Grinyer, E. G. Fuakye, G. Hackman, J. Hollett, R. Jain, and et al., "First direct measurement of 59cu(p,α)56ni: A step towards constraining the ni-cu cycle in the cosmos," *Physical Review. C*, vol. 104, 10 2021.

[82] N. Bhathi, J. S. Randhawa, R. Kanungo, J. Refsgaard, M. Alcorta, T. Ahn, C. Andreoiu, D. Bardayan, S. S. Bhattacharjee, B. Davids, G. Christian, A. A. Chen, R. Coleman, P. E. Garrett, G. F. Grinyer, E. G. Fuakye, G. Hackman, R. Jain, K. Kapoor, R. Krücken, A. Laffoley, A. Lennarz, J. Liang, Z. Meisel, A. Psaltis, A. Radich, M. Rocchini, J. S. Rojo, N. Saei, M. Saxena, M. Singh, C. E. Svensson, P. Subramaniam, A. Talebitaher, S. Upadhyayula, C. Waterfield, J. Williams, M. Williams, and M. A. Zubair, "Direct measurement of 59cu(p,α)56ni precludes a strong nicu cycle in type-i x-ray bursts," *The Astrophysical Journal*, vol. 999, p. 8, feb 2026.

[83] G. Owens-Fryar, S. M. Lyons, A. L. Richard, A. Spyrou, B. A. Brown, C. E. P. Robin, Z. Meisel, H. C. Berg, A. Chester, A. A. Chen, B. Crider, P. A. DeYoung, P. Gastis, E. C. Good, C. Harris, K. Hermansen, S. N. Liddick, A. Palmisano-Kyle, A. Psaltis, M. K. Smith, E. Rubino, S. K. Subedi, I. Sultana, and A. Tsantiri, "Total absorption spectroscopy for the β^+ decay strength distribution of ^{60}Ga," *Phys. Rev. C*, vol. 111, p. 065801, Jun 2025.

[84] D. Morrissey, B. Sherrill, M. Steiner, A. Stolz, and I. Wiedenhoever, "Commissioning the a1900 projectile fragment separator," *Nuclear Instruments and Methods in Physics Research Section B: Beam Interactions with Materials and Atoms*, vol. 204, pp. 90–96, 2003. 14th International Conference on Electromagnetic Isotope Separators and Techniques Related to their Applications.

[85] P. A. Závodszky, B. Arend, D. Cole, J. DeKamp, M. Doleans, G. Machicoane, F. Marti, P. Miller, J. Moskalik, W. Nurnberger, J. Ottarson, J. Vincent, X. Wu, and A. Zeller, "Design, construction, and first commissioning results of superconducting source for ions at nscl/msua)," *Review of Scientific Instruments*, vol. 79, p. 02A302, 01 2008.

[86] P. A. Zavodszky, H. Koivisto, D. Cole, and P. Miller, "Emittance studies of artemis-the new ecr ion source for the coupled cyclotron facility at nscl/msu," *AIP Conference Proceedings*, vol. 576, pp. 619–622, 07 2001.

[87] D. Bazin, V. Andreev, A. Becerril, M. Doléans, P. Mantica, J. Ottarson, H. Schatz, J. Stoker, and J. Vincent, "Radio frequency fragment separator at nscl," *Nuclear Instruments and Methods in Physics Research Section A: Accelerators, Spectrometers, Detectors and Associated Equipment*, vol. 606, no. 3, pp. 314–319, 2009.

[88] A. C. Dombos, *β-decay Total Absorption Spectroscopy Around A=100-110 Relevant to Nuclear Structure and the Astrophysical R Process*. PhD thesis, Michigan State University, 2018.

[89] A. Simon, S. Quinn, A. Spyrou, A. Battaglia, I. Beskin, A. Best, B. Bucher, M. Couder, P. DeYoung, X. Fang, J. Görres, A. Kontos, Q. Li, S. Liddick, A. Long, S. Lyons, K. Padmanabhan, J. Peace, A. Roberts, D. Robertson, K. Smith, M. Smith, E. Stech, B. Stefanek, W. Tan, X. Tang, and M. Wiescher, "Sun: Summing nai(tl) gamma-ray detector for capture reaction measurements," *Nuclear Instruments and Methods in Physics Research Section A: Accelerators, Spectrometers, Detectors and Associated Equipment*, vol. 703, pp. 16–21, 2013.

[90] C. Mazzocchi, Z. Janas, J. Döring, M. Axiotis, L. Batist, R. Borcea, D. Cano-Ott, E. Caurier, G. de Angelis, E. Farnea, A. Faßbender, A. Gadea, H. Grawe, A. Jungclaus, M. Kapica, R. Kirchner, J. Kurcewicz, T. Lenzi, S.M.and Martínez, I. Mukha, E. Nácher, D. Napoli, E. Roeckl, B. Rubio, R. Schwengner, T. J.L., and C. Ur, "First measurement of β-decay properties of the proton drip-line nucleus 60ga," *The European Physical Journal A - Hadrons and Nuclei*, vol. 12, p. 269–277, 2001.

[91] S. Agostinelli, J. Allison, K. Amako, J. Apostolakis, H. Araujo, P. Arce, M. Asai, D. Axen, S. Banerjee, and G. e. a. Barrand, "Geant4 — a simulation toolkit," *Nuclear Instruments and Methods in Physics Research Section A: Accelerators, Spectrometers, Detectors and Associated Equipment*, vol. 506, no. 3, pp. 250–303, 2003.

[92] S. J. Quinn, *CAPTURE CROSS SECTIONS FOR THE ASTROPHYSICAL P PROCESS*. PhD thesis, Michigan State University, 2015.

[93] National Nuclear Data Center, Evaluated Nuclear Structure Data File (ENSDF) Retrieval, www.nndc.bnl.gov, 2012.

[94] S. E. A. Orrigo, B. Rubio, W. Gelletly, P. Aguilera, A. Algora, A. I. Morales, and et al., "β decay of the very neutron-deficient ^{60}Ge and ^{62}Ge nuclei," *Phys. Rev. C*, vol. 103, p. 014324, Jan 2021.

[95] Kucuk, L., Orrigo, S. E. A., Montaner-Pizá, A., Rubio, B., Fujita, Y., Gelletly, W., Blank, B., Oktem, Y., Adachi, T., Algora, A., Ascher, P., Cakirli, R. B., de France, G., Fujita, H., Ganioğlu, E., Giovinazzo, J., Grévy, S., Marqués, F. M., Molina, F., de Oliveira Santos, F., Perrot, L., Raabe, R., Srivastava, P. C., Susoy, G., Tamii, A., and Thomas, J. C., "Half-life determination of tz = -1 and tz = - $\frac{1}{2}$ proton-rich nuclei and the β decay of 58zn," *Eur. Phys. J. A*, vol. 53, no. 6, p. 134, 2017.

[96] J. Hardy, L. Carraz, B. Jonson, and P. Hansen, "The essential decay of pandemonium: A demonstration of errors in complex beta-decay schemes," *Physics Letters B*, vol. 71, no. 2, pp. 307–310, 1977.

[97] L. Kirsch and L. Bernstein, "Rainier: A simulation tool for distributions of excited nuclear states and cascade fluctuations," *Nuclear Instruments and Methods in Physics Research Section A: Accelerators, Spectrometers, Detectors and Associated Equipment*, vol. 892, pp. 30–40, 2018.

[98] R. Capote, M. Herman, P. Obložinský, P. G. Young, and S. e. a. Goriely, "Ripl – reference input parameter library for calculation of nuclear reactions and nuclear data evaluations," *Nuclear Data Sheets*, vol. 110, no. 12, pp. 3107–3214, 2009. Special Issue on Nuclear Reaction Data.

[99] A. Poves, J. Sanchez-Solano, E. Caurier, and F. Nowacki, "Shell model study of the isobaric chains A = 50, A = 51 and A = 52," *Nucl. Phys. A*, vol. 694, pp. 157–198, 2001.

[100] M. Honma, T. Otsuka, B. A. Brown, and T. Mizusaki, "Effective interaction for pf-shell nuclei," *Phys. Rev. C*, vol. 65, p. 061301, May 2002.

[101] T. Marketin, D. Vretenar, and P. Ring, "Calculation of β-decay rates in a relativistic model with momentum-dependent self-energies," *Phys. Rev. C*, vol. 75, p. 024304, Feb 2007.

[102] G. A. Lalazissis, J. König, and P. Ring, "New parametrization for the lagrangian density of relativistic mean field theory," *Phys. Rev. C*, vol. 55, pp. 540–543, Jan 1997.

[103] C. Robin and E. Litvinova, "Nuclear response theory for spin-isospin excitations in a relativistic quasiparticle-phonon coupling framework," *Eur. Phys. J. A*, vol. 52, no. 7, p. 205, 2016.

[104] C. Robin and E. Litvinova, "Coupling charge-exchange vibrations to nucleons in a relativistic framework: effect on Gamow-Teller transitions and β-decay half-lives," *Phys. Rev. C*, vol. 98, no. 5, p. 051301, 2018.

[105] M. Guttormsen, A. C. Larsen, S. N. Liddick, E. Lima, A. H. Mjøs, A. Spyrou, and F. Zeiser, "Unfolding of excitation-energy spectra from total absorption γ-ray spectroscopy for the β-oslo method." preprint.

[106] M. Guttormsen, T. Tveter, L. Bergholt, F. Ingebretsen, and J. Rekstad, "The unfolding of continuum γ-ray spectra," *Nuclear Instruments and Methods in Physics Research Section A: Accelerators, Spectrometers, Detectors and Associated Equipment*, vol. 374, no. 3, pp. 371–376, 1996.

[107] M. Guttormsen, T. Ramsøy, and J. Rekstad, "The first generation of γ-rays from hot nuclei," *Nuclear Instruments and Methods in Physics Research Section A: Accelerators, Spectrometers, Detectors and Associated Equipment*, vol. 255, no. 3, pp. 518–523, 1987.

[108] J. E. Midtbø, F. Zeiser, E. Lima, A.-C. Larsen, G. M. Tveten, M. Guttormsen, F. L. Bello Garrote, A. Kvellestad, and T. Renstrøm, "A new software implementation of the oslo method with rigorous statistical uncertainty propagation," *Computer Physics Communications*, vol. 262, p. 107795, 2021.

[109] A. Schiller, L. Bergholt, M. Guttormsen, E. Melby, J. Rekstad, and S. Siem, "Extraction of level density and γ strength function from primary γ spectra," *Nuclear Instruments and Methods in Physics Research Section A: Accelerators, Spectrometers, Detectors and Associated Equipment*, vol. 447, no. 3, pp. 498–511, 2000.

[110] D. Soltesz, M. A. A. Mamun, A. V. Voinov, Z. Meisel, B. A. Brown, C. R. Brune, S. M. Grimes, H. Hadizadeh, M. Hornish, T. N. Massey, J. E. O'Donnell, and W. E. Ormand, "Determination of the ^{60}Zn level density from neutron evaporation spectra," *Phys. Rev. C*, vol. 103, p. 015802, Jan 2021.

[111] A. C. Larsen, M. Guttormsen, N. Blasi, A. Bracco, F. Camera, L. C. Campo, T. K. Eriksen, A. Görgen, T. W. Hagen, and V. W. e. a. Ingeberg, "Low-energy enhancement and fluctuations of γ-ray strength functions in 56,57fe: test of the brink–axel hypothesis," *Journal of Physics G: Nuclear and Particle Physics*, vol. 44, p. 064005, apr 2017.

[112] K. Nilson, B. Erlandsson, and A. Marcinkowski, "Gamma-ray strength function measurements for 59co, 61cu and 62cu," *Nuclear Physics A*, vol. 391, no. 1, pp. 61–71, 1982.

[113] B. Erlandsson, K. Nilson, and A. Marcinkowski, "Investigation of the γ-ray strength function in 64, 66zn by means of the average resonance method," *Nuclear Physics A*, vol. 343, pp. 197–209, 1980.

[114] H. Utsunomiya, T. Renstrøm, G. M. Tveten, S. Goriely, S. Katayama, T. Ari-izumi, D. Takenaka, D. Symochko, B. V. Kheswa, V. W. Ingeberg, T. Glodariu, Y.-W. Lui, S. Miyamoto, A. C. Larsen, J. E. Midtbø, A. Görgen, S. Siem, L. C. Campo, M. Guttormsen, S. Hilaire, S. Péru, and A. J. Koning, "Photoneutron cross sections for ni isotopes: Toward understanding (n, γ) cross sections relevant to weak s-process nucleosynthesis," *Phys. Rev. C*, vol. 98, p. 054619, Nov 2018.

[115] A. Gelman, J. B. Carlin, H. S. Stern, D. B. Dunson, A. Vehtari, and D. B. Rubin, *Bayesian Data Analysis*. Chapman & Hall/CRC, 2013.

[116] D. MacKay, *InformationTheory, Inference, and Learning Algorithms*, vol. 50. Cambridge University Press, 01 2003.

[117] W. W. Wood, "A brief history of the use of the metropolis method at lanl in the 1950s," *AIP Conference Proceedings*, vol. 690, no. 1, p. 39–44, 2003.

[118] S. Goriely, S. Hilaire, and A. J. Koning, "Improved microscopic nuclear level densities within the hartree-fock-bogoliubov plus combinatorial method," *Phys. Rev. C*, vol. 78, p. 064307, Dec 2008.

[119] T. RAUSCHER and F.-K. THIELEMANN, "Tables of nuclear cross sections and reaction rates: An addendum to the paper "astrophysical reaction rates from statistical model calculations"," *Atomic Data and Nuclear Data Tables*, vol. 79, no. 1, pp. 47–64, 2001.

[120] R. H. Cyburt, A. M. Amthor, R. Ferguson, Z. Meisel, K. Smith, S. Warren, A. Heger, R. D. Hoffman, T. Rauscher, A. Sakharuk, H. Schatz, F. K. Thielemann, and M. Wiescher, "The jina reaclib database: Its recent updates and impact on type-i x-ray bursts," *The Astrophysical Journal Supplement Series*, vol. 189, p. 240, jun 2010.

[121] D. Soltesz, M. A. A. Mamun, A. V. Voinov, Z. Meisel, B. A. Brown, C. R. Brune, S. M. Grimes, H. Hadizadeh, M. Hornish, T. N. Massey, J. E. O'Donnell, and W. E. Ormand, "Determination of the ^{60}Zn level density from neutron evaporation spectra," *Phys. Rev. C*, vol. 103, p. 015802, Jan 2021.

[122] E. Lopez-Saavedra, M. L. Avila, W. J. Ong, P. Mohr, S. Ahn, H. Arora, L. Balliet, K. Bhatt, S. M. Cha, K. A. Chipps, J. Dopfer, I. A. Tolstukhin, R. Jain, M. J. Kim, K. Kolos, F. Montes, D. Neto, S. D. Pain, J. Pereira, J. S. Randhawa, L. J. Sun, C. Ugalde, and L. Wagner, "Detailed study of the ^{59}cu(p,α)^{56}ni reaction and constraints on its astrophysical reaction rate," 2026.

[123] G. O. Roberts, A. Gelman, and W. R. Gilks, "Weak convergence and optimal scaling of random walk Metropolis algorithms," *The Annals of Applied Probability*, vol. 7, no. 1, pp. 110 – 120, 1997.

[124] S. Brooks, A. Gelman, G. Jones, and X.-L. Meng, eds., *Handbook of Markov chain Monte Carlo*. Chapman & Hall/CRC Handbooks of Modern Statistical Methods, Philadelphia, PA: Chapman & Hall/CRC, Jun 2010.

[125] H. Robbins and S. Monro, "A Stochastic Approximation Method," *The Annals of Mathematical Statistics*, vol. 22, no. 3, pp. 400 – 407, 1951.

[126] G. E. P. Box, G. M. Jenkins, and G. C. Reinsel, *Time series analysis : forecasting and control*. Hoboken, N.J.: John Wiley, 2008.

[127] J. Noble, "What is a gaussian mixture model?," Nov 2025.

[128] Scikit-learn Developers, "Mixture models (gmm)," 2024.

[129] Scikit-learn Developers, "Gaussianmixture," 2024.

[130] A. M. Edwards and M. Auger-Méthé, "Using highest density intervals can reduce perceived uncertainty in stock assessments," *Fisheries Research*, vol. 285, p. 107326, 2025.

[131] J. K. Kruschke, "Chapter 4 - what is this stuff called probability?," in *Doing Bayesian Data Analysis (Second Edition)* (J. K. Kruschke, ed.), pp. 71–97, Boston: Academic Press, second edition ed., 2015.

APPENDIX

.1 Additional Features Included in the Metroplis-Hastings Algorithm

Beyond the base MH algorithm described in Sec.6.2, several features were included to improve the quality of the posterior parameter set, leading to a more robust fit. The use of the tool is meant to be an iterative process, to guide the user's decision making process to choose reasonable hyper-parameters that will give sensible and physically justifiable results.

.1.1 Covariance Scaling

In 1997, Roberts, Gelman, and Gilks determined that the variance of the proposal has a strong impact on both the speed of convergence as well as the overall acceptance [123]. Through formal proof they conclude that the algorithm can be optimized by scaling the parameter covariance matrix by a factor of $2.38^2/d$, where d is the dimensions of the matrix. In practice, the covariance matrix is first generated from user defined hyper parameters and check is performed to ensure that it is positive definite. Then the scaling condition from Roberts et al. is applied.

.1.2 Block Proposals

Since some parameters are correlated, the efficiency can be further improved by creating parameter groups called blocks. This is of particular importance for modeling the γSF as both E1 and M1 parameters are fit simultaneously. While parameters can be grouped however the user wishes, it is recommended to begin by separating them into two blocks:

$$E = (w, E, f), \qquad M = (upbendc, upbende, upbendf, beta2),$$

, in order to understand the general qualities of the E1 and M1 parameters. Borrowing ideas from Gibbs sampling methods [115], the MH sampler designed for this work updates each block sequentially, which is helpful when the when the scale of the parameters differs between blocks. With this in mind, the user is encouraged to further separate the M1 block group into

$$M_1 = (upbendc) \qquad M_2 = (upbende, upbendf, beta2)$$

as the upbendc parameter range is 5-6 orders of magnitude smaller than the other M1 parameters. For each block of dimension d, the proposal is

$$\boldsymbol{\theta}' = \boldsymbol{\theta} + Lz, \qquad z \sim \mathcal{N}(\mathbf{0}, I_d),$$

where L is the Cholesky factor of the proposal covariance:

$$\Sigma_{\text{prop}} = LL^{\top}.$$

and I_d is the identity matrix with d dimensions. The Cholesky factorization will then improve the performance of the correlated parameters in each block [124].

.1.3 Adaptive Tuner

Another significant addition is an adaptive step size tuner applied in the burn phase of the MH. After a user defined interval of steps, the algorithm compares the current acceptance ratio to the target and approximates a scaling that will guide the steps toward the optimal acceptance ratio. Referencing the stochastic approximation method developed by Robbins and Monro [125]

$$x_{n+1} = x_n + b_n(A_n - a^*)$$

where, in the context of this problem, x is proposed scalings to the Cholesky factor L, A_n is the acceptance ratio of the block within the interval, and a^* is the target acceptance ratio for the block. b_n functions as a gain that mediates convergence speed, stability, and sensitivity to noise. In order to ensure that the proposed multiplicative scale is positive, let

$$x_n = log(\alpha_n)$$

then exponentiating,

$$\alpha_{n+1} = \alpha_n \, exp[b_n(A_n - a^*)]$$

A first order Taylor expansion gives

$$\alpha_{n+1} \approx \alpha_n[1 + (A_n + a^*)]$$

Once the burn phase is complete, the adaptation stops, making the scale constant in the recording phase. This is done to maintain detailed balance and ergodicity.

.1.4 Two Phase ....

The last major update to the base MH algorithm is making it calculate the posterior distribution twice; first in a shorter exploratory pilot run, and later in a longer production run. In the pilot run, covariance matrices are constructed by guessing the parameter means and covariances. The MH sampler then explores the parameter space based on that assumption and builds new "evidence based" covariance matrices for each block, which are calculated from the posterior distribution. These evidence based covariances are used in the production run, providing improvements in parameter space exploration, or mixing, and acceptance ratio.

.2 Diagnostic Tools

To check the mixing of the posterior parameters, the code uses the Effective Sample Size (ESS) diagnostic. This check is derived from the autocorrelation or independence of the posterior for each parameter. Posterior samples generated by MH are not independent, since new steps are calculated from the previous. As the step sizes are typically small, the posterior can be autocorrelated, meaning that the normalized covariance is high. For a parameter chain $x_1, x_2, ..., x_N$, the autocorrelation ρ is defined as[126]

$$\rho_k = \frac{Cov(x_i, x_{i+k})}{Var(x)}$$

where i is the initial position, k is the lag or number of steps between the initial position and testing position. Cov is the scalar covariance and Var is the variance of the entire posterior of the parameter. Autocorrelation can increase as the MH sampler rejects parameter proposals, since rejection saves the previous step's accepted parameter set, reducing the ratio of independent samples to total number of acceptances. The integrated autocorrelation time τ_{int} describes how the entire posterior is correlated.

$$\tau_{int} = 1 + 2\sum_{k=1}^{\infty}\rho_k$$

τ_{int} is can be understood as approximately the number of iterations needed to have an independent sample. To find the ESS[115]

$$ESS = \frac{N}{\tau_{int}}$$

where N is the total number of samples in the posterior. The ESS tells the user how many independent samples the calculated posterior is equivalent to. Ideally, $\tau_{int}/ESS << .1$. This shows that there are many independent draws within the posterior, and the parameter is mixing well. Including the additional features in the MH was for the purpose of improving this ratio.

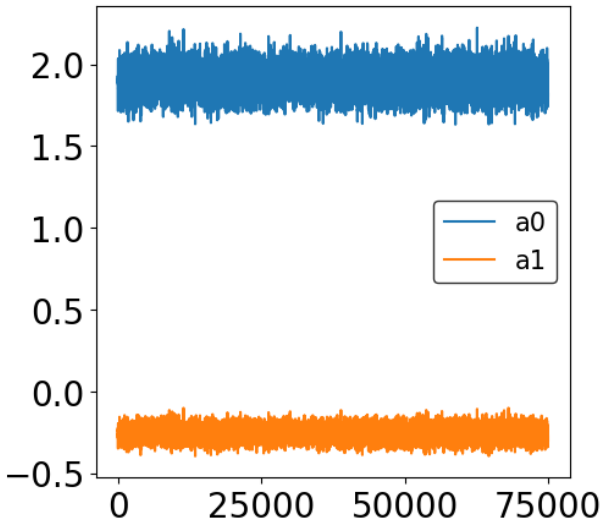

Figure .1 A plot of ctable and ptable walkers over ≈ 80 000 steps. There are no large fluctuations, indicating that both parameters converged during the burn phase.

.3 Data Visualization tools

After the algorithm has done its work finding model parameters that describe the data, it is important to see how the parameter values are distributed, if they converged, and how well the parameters fit the data. To address these needs, several visualization tools were developed.

Walker The walker [fig.1] shows the value of each parameter at each step of the calculation phase. This plot is very useful for checking whether the parameters converged at the end of the algorithm. If a parameter does not converge by the end of the trial, this suggests more calculation steps are needed It also gives an idea of the variation of the individual parameters and how the group changes together.

χ^2 vs Single Parameter plot In these plots a single parameter a_i is compared with the associated χ^2 of its parameter group. From this the range of accepted parameter values can be determined.

Taking the ratio of the range of a_i with some other parameter a_j can help to determine the relative step size between the two. Comparing each parameter to a_i allows the step size of each parameter to be put in terms of a_i step size, therefore only the step step size of a_i needs to be chosen in subsequent trials. This plot also shows a line at the parameter value of the minimum χ^2. In future runs, this value could be used as an initial guess for the algorithm to better explore that region.

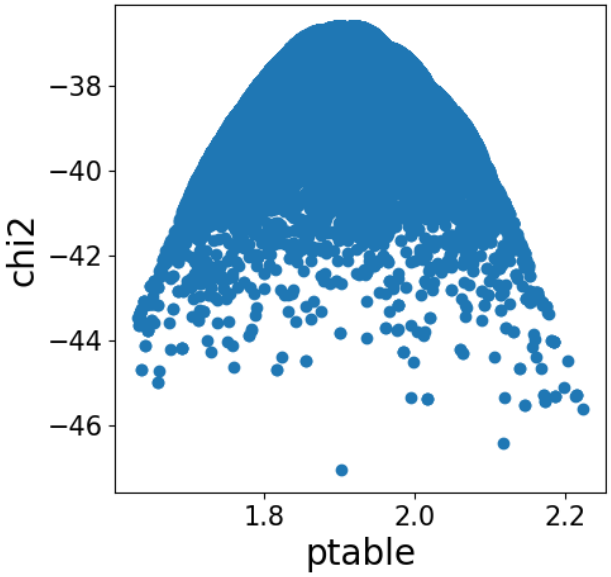

Figure .2 Example distribution of accepted posterior p table value with respect to the χ^2 value.

χ^2 vs Parameter a_i vs Parameter a_j plot This 3D visualization tool compares two parameters with the χ^2 of the full parameter set. This gives a more complete description of the region being explored and can show other local χ^2 minima that can be explored with appropriate initial parameter choices.

Corner plot The corner plot is a set of two dimensional contour plots that compare parameter distributions with one another. The shape of the contour ... how the parameters change with respect to one another. The rings of the plot show areas of greater probability, with the central, darkest rings being the most probable region in the 2 parameter space. The corner plot also displays the one parameter distribution.

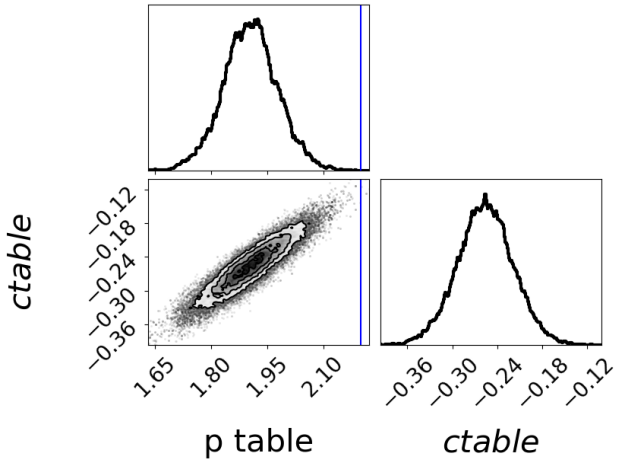

Figure .3 Example corner plot of posterior p table and c table parameter distributions. The top and right histograms project the parameter density of the p table and c table parameters respectively. The center plot is the 2D representation of the full posterior.

.3.1 Handling Multi-modal Distributions

It is possible for the Metropolis-Hastings algorithm to find multiple sets of parameter posteriors that fit the data well. This is displayed in the previous visualization tools as multiple peaks in the χ^2 plots and multiple contours in the corner plot. In such case, taking the median of the full set of parameters can lead to incorrect conclusions on what parameters best represent the data. Each mode should be handled independently to accurately visualize how well the sets of parameters represent the data. This can done in many ways including creating parameter gates or

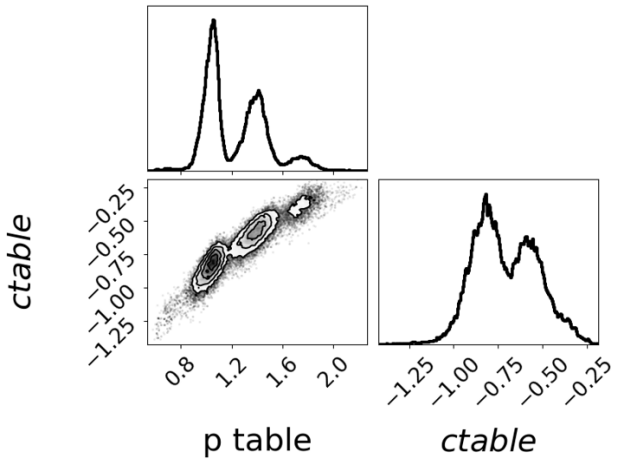

Figure .4 An example of a trimodal distribution. The top right mode has low statistics; but, is still an independent cluster of solutions.

using Gaussian Mixture Modeling (GMM) with Bayesian Information Criterion (BIC) to represent the posterior as a combination of gaussians. For this work, GMM + BIC was used. For plotting, the GMM+BIC regions are grouped into clusters, which are treated as High Density Intervals (HDI) to determine the median and CI for each solution group.

.3.1.1 Gaussian Model Mixing (GMM)

GMM is an unsupervised learning method that assumes a dataset is from a finite number of gaussian distributions with unknown mean, variance, and mixing parameters[127]. The mean and variance are the usual definitions. The mixing parameter is the probability that a data point d was generated by gaussian g. In this way, every data point is assigned to a gaussian, creating a cluster of points. In this work, the gaussians from GMM are used to determine how many modes (solution groups) exist within the posterior distribution. It important to separate these groups because the resulting median and CI each can lead to different conclusions about the function (e.g. NLD, γSF) being fit. To perform GMM, the `sklearn.mixure` library was imported and GaussianMixture objects were constructed [128]. This class estimates how data in multi-dimensional posterior parameter distributions can be organized into different gaussian shaped regions.

.3.1.2 Bayesian Information Criterion (BIC)

In the context of this work, BIC is used to determine the minimum number of gaussian functions needed to represent the posterior parameter distribution. Formally

$$BIC = kln(n) - 2ln(\hat{L})$$

. Contextually, k is the number of gaussians used by GMM, n is the sample size, and $\hat{L}$ is the maximized likelihood of the GMM at k(maybe???). By looping over the GaussianMixture objects from scikit[129] with various values of k, we calculate the BIC for each and choose the value of k with the lowest BIC (k_{min}) to be the number of gaussian distributions needed to represent the parameter space. It is important to check that k_{min} is not equal to the maximum value of k used in GMM, as the minimum BIC may not have been found.

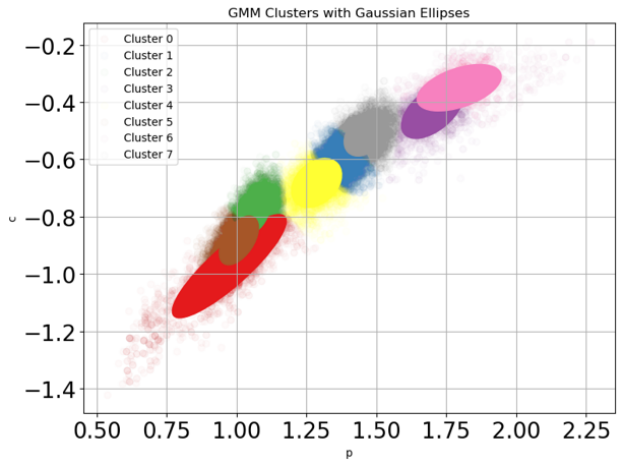

Figure .5 Visualization of the minimum number of gaussians needed to represent the the trimodal posterior distribution in fig..4. Each color is a different cluster of data.

Visualization Once k_{min} has been determined, a color coded overlay plot of the k_{min} distributions on to the data [fig..5] can be made. This is useful for seeing how the posterior samples are clustered by GMM. It is often the case that multiple gaussian regions are used to represent one posterior cluster. These regions can be grouped together by the user into a single object that will be used.

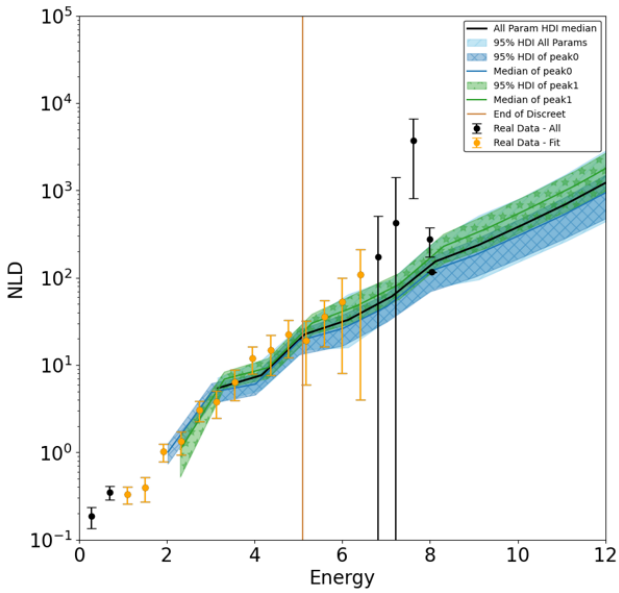

Figure .6 The HDI of the NLD for two largest modes are shown here. Peak0 in blue is the bottom left mode and Peak1 in green is the center mode in [fig..4]. At high energies, the two modes have upto an order of magnitude of difference. The thrid mode was excluded due to its lack of statistics.

.3.1.3 Highest Density Intervals (HDI)

Since the clusters are a sum of N gaussian distributions, the usual method of finding a CI based on percentiles is not valid. That method assumes that the mean value of the distribution is centered and the width is symmetric about the mean. This is not the case for multi modal posterior distributions. The posterior distributions are skewed, so the upper and lower 2.5 percentile slices may remove probable parameter values[130]. The HDI specifies the parameter range where most (e.g. 68% , 95%) of the probability density is located. For one parameter,

$$\int_{x:p(x)>W} dx\ p(x) = percentage\ of\ distribution$$

where W is some minimum value, p(x) is the parameter distribution function and x is the parameter value[131]. The parameter sets in multidimensional HDI regions are used in the model to calculate the CI for the cluster.